JEM Journal of Experimental Medicine

ARTICLE

Protection of ischemic white matter and oligodendrocytes in mice by 3K3A-activated protein C

Mikko T. Huuskonen[1,2*], Yaoming Wang[1,2*], Angeliki Maria Nikolakopoulou[1,2*], Axel Montagne[1,2*], Zhonghua Dai[1,2], Divna Lazic[1,2], Abhay P. Sagare[1,2], Zhen Zhao[1,2], Jose A. Fernandez[3], John H. Griffin[3,4], and Berislav V. Zlokovic[2]

Subcortical white matter (WM) stroke accounts for 25% of all strokes and is the second leading cause of dementia. Despite such clinical importance, we still do not have an effective treatment for ischemic WM stroke, and the mechanisms of WM postischemic neuroprotection remain elusive. 3K3A-activated protein C (APC) is a signaling-selective analogue of endogenous blood protease APC that is currently in development as a neuroprotectant for ischemic stroke patients. Here, we show that 3K3A-APC protects WM tracts and oligodendrocytes from ischemic injury in the corpus callosum in middle-aged mice by activating protease-activated receptor 1 (PAR1) and PAR3. We show that PAR1 and PAR3 were also required for 3K3A-APC's suppression of post–WM stroke microglia and astrocyte responses and overall improvement in neuropathologic and functional outcomes. Our data provide new insights into the neuroprotective APC pathway in the WM and illustrate 3K3A-APC's potential for treating WM stroke in humans, possibly including multiple WM strokes that result in vascular dementia.

Introduction

White matter (WM) injury is present in most stroke patients (Matute et al., 2013; Wang et al., 2016a; Feigin et al., 2018; Marin and Carmichael, 2018). Moreover, stroke in small brain vessels occurring in subcortical WM regions accounts for 25% of all strokes and is the second leading cause of dementia (Bos et al., 2018; Iadecola and Gottesman, 2018; Wardlaw et al., 2019; Wardlaw et al., 2015). The incidence of WM strokes is increased with age (de Leeuw et al., 2001; Iadecola, 2017; Kapasi et al., 2017; Matute et al., 2013; Wardlaw et al., 2019). WM tracts in the corpus callosum (CC) are frequently affected by WM disease and WM strokes, leading to vascular dementia (DeCarli et al., 2005; Marin and Carmichael, 2019). Besides affecting cognition, WM strokes are associated with abnormalities in balance and gait and carry an increased risk of death (Debette and Markus, 2010; Siegel et al., 2016; Zheng et al., 2011). Despite such clinical importance, we still do not have an effective treatment for ischemic WM stroke, and the mechanisms of postischemic WM neuroprotection remain elusive (Marin and Carmichael, 2018; Marin and Carmichael, 2019; Wardlaw et al., 2019). Only recently, focal WM stroke models in the CC (Rosenzweig and Carmichael, 2013; Sozmen et al., 2019; Sozmen et al., 2009; Sozmen et al., 2016) and/or internal capsule (Uchida et al., 2015) have been developed, allowing us to study the mechanisms of WM injury and protection.

Activated protein C (APC) is an endogenous circulating plasma protease generated from protein C zymogen by thrombin cleavage on endothelial cells (Griffin et al., 2018). APC has two distinct activities: (a) anticoagulant based on limited proteolysis of coagulation factors Va and VIIIa; and (b) cell signaling that requires proteolytic activation of protease-activated receptor 1 (PAR1) and interactions with other receptors resulting in vasculoprotection, neuroprotection, and antiinflammatory activities (Griffin et al., 2016; Griffin et al., 2015; Griffin et al., 2018). APC is beneficial in rodent models of neurologic disorders including large artery infarcts (Cheng et al., 2003; Cheng et al., 2006; Liu et al., 2004; Zlokovic et al., 2005), multiple sclerosis (Han et al., 2008), amyotrophic lateral sclerosis (ALS; Shi et al., 2019; Winkler et al., 2014; Zhong et al., 2009), and Alzheimer's disease (AD; Lazic et al., 2019). It is also protective in models of sepsis, ischemic heart, kidney and liver injury, diabetes, organ transplants, wound healing, graft-versus-host disease, and radiation, as reviewed elsewhere (Griffin et al., 2015;

[1]Department of Physiology and Neuroscience, Keck School of Medicine of the University of Southern California, Los Angeles, CA; [2]The Zilkha Neurogenetic Institute, Keck School of Medicine of the University of Southern California, Los Angeles, CA; [3]Department of Molecular Medicine, The Scripps Research Institute, La Jolla, CA; [4]Division of Hematology/Oncology, Department of Medicine, University of California, San Diego, San Diego, CA.

*M.T. Huuskonen, Y. Wang, A.M. Nikolakopoulou, and A. Montagne contributed equally to this paper; Correspondence to Berislav V. Zlokovic: zlokovic@usc.edu.

Griffin et al., 2018). APC and its signaling-selective analogues engineered with reduced anticoagulant activity but preserved cell-signaling activities require, besides PAR1, the endothelial protein C receptor (EPCR) on endothelium for endothelial cell protection (Cheng et al., 2003; Griffin et al., 2018; Guo et al., 2009a; Guo et al., 2009b) and PAR3 on neurons for direct neuron protection (Guo et al., 2004; Guo et al., 2009a; Guo et al., 2009b). APC's effects and its receptors on oligodendrocytes and in the WM have not been studied, and its effects on microglia and astrocyte responses are still relatively poorly understood.

3K3A-APC (Lys191-193Ala), a signaling-selective APC analogue (Guo et al., 2013; Mosnier et al., 2007; Sinha et al., 2018) with greatly diminished (<10%) anticoagulant activity (Mosnier et al., 2004), is highly protective in rodent models of large artery infarcts, and it reduces risk for intracerebral bleeding (Guo et al., 2009a; Guo et al., 2009b; Wang et al., 2012; Wang et al., 2013; Wang et al., 2016b). 3K3A-APC is protective in rodent models of brain injury (Walker et al., 2010), including ALS (Shi et al., 2019; Zhong et al., 2009) and multiple sclerosis (Han et al., 2008). Importantly, 3K3A-APC has an established safety and pharmacokinetic profile in humans (Lyden et al., 2013; Williams et al., 2012), and it reduces intracerebral bleeding in ischemic stroke patients as shown in a phase 2 clinical trial (Lyden et al., 2019). Using a model of WM stroke generated by vasoconstriction in the CC in middle-aged mice (Rosenzweig and Carmichael, 2013; Sozmen et al., 2019; Sozmen et al., 2009; Sozmen et al., 2016), we show here that 3K3A-APC protects the WM tracts and oligodendrocytes from ischemic injury by activating PAR1 and PAR3. We show that PAR1 and PAR3 were also required for 3K3A-APC's suppression of post–WM stroke microglia and astrocyte responses and for overall improvement in neuropathologic and functional outcomes. These new data provide further insight into the neuroprotective APC pathway in the WM, and they support further development of 3K3A-APC as a potential therapy to prevent and/or treat WM stroke in humans, possibly including multiple WM strokes that lead to vascular dementia (Wardlaw et al., 2019).

Results

3K3A-APC reduces lesion volume and improves functional outcome after WM stroke

WM stroke was produced by stereotaxic injections of N^5-(1-iminoethyl)-L-ornithine (L-Nio; 30 mg/ml; Millipore) into the CC, which produces intense vasoconstriction at the site of injection, leading to focal ischemia, as previously described (Rosenzweig and Carmichael, 2013; Sozmen et al., 2019; Sozmen et al., 2009; Sozmen et al., 2016). We used the L-Nio model to induce WM stroke because the lesion site is localized reproducibly to the CC and does not spread to gray-matter regions, which might potentially interfere with the WM postischemic process and repair. Although large artery stroke models including middle cerebral artery occlusion and embolic stroke may also affect the WM, the degree of WM involvement varies from mouse to mouse and treatment applied. This makes it difficult not only to isolate the effects of gray-matter stroke on the WM postischemic process, but also to generate reproducibly the topographic maps of affected WM regions for cellular and molecular studies.

Murine recombinant 3K3A-APC (0.2 mg/kg) or vehicle was administered to L-Nio stroke mice via tail vein 4 h and 1, 2, 3 and 4 d after stroke (Fig. 1 A). Control mice underwent a surgical sham procedure for craniotomy similar to that of L-Nio stroke mice. In a separate test group, mice received vehicle injections into the CC. In contrast to L-Nio, injections of vehicle into the CC did not result in a detectable lesion in the CC on day 1 or 7 after injection (data not shown). Vehicle injections into the CC were not performed in control experiments.

Longitudinal T2-weighted magnetic resonance imaging (MRI) indicated 64 and 66% reductions in CC lesion volume after 3K3A-APC treatment compared with vehicle on days 1 and 7 after stroke, respectively (Fig. 1, B and C). This was confirmed by histologic analysis of lesion volume with Cresyl Violet stain on coronal brain sections (Fig. 1, D and E). There was strong positive correlation between lesion volume determined by MRI and Cresyl Violet stain, as shown 7 d after stroke (Fig. S1). Adhesive-removal and grid-walking tests (Fig. 1, F and G) indicated substantial improvement in sensorimotor and motor functions, respectively, in 3K3A-APC–treated compared with vehicle-treated mice on day 7 after stroke.

3K3A-APC protects blood–brain barrier (BBB) integrity after WM stroke

Maps and values of the BBB permeability transfer constant, K_{trans}, for gadolinium-based contrast agent were computed from dynamic contrast enhanced (DCE) MRI scans as previously described (Montagne et al., 2018; Nikolakopoulou et al., 2019). The DCE-MRI analysis revealed a pronounced in vivo BBB breakdown in the CC in vehicle-treated mice 1 d after stroke that persisted for 7 d, was reduced by 3K3A-APC by 35% on day 1 after stroke, and was back to normal values comparable to those in sham-operated controls on day 7 after stroke (Fig. 2, A and B). Postmortem tissue analysis revealed that 3K3A-APC reduced accumulation of blood-derived fibrinogen (340 kD) and IgG (150 kD) extravascular deposits (Fig. 2, C–F) by 36–43% on day 1 after stroke, and these were almost back to control values of sham-operated mice on day 7 after stroke.

3K3A-APC protects the WM tracts and prevents myelin loss after ischemic stroke

Echo planar imaging/diffusion-tensor imaging (EPI/DTI) MRI fiber tracking (Montagne et al., 2018) was used to visualize WM tracts in vivo (Fig. 3 A) and suggested a 48% loss in CC tract volumes in vehicle-treated mice 1 and 7 d after stroke relative to sham-operated controls, which was almost completely restored by 3K3A-APC (Fig. 3 B). Immunostaining for myelin basic protein (MBP; Fig. 3 C) indicated 74% and 79% loss of MBP signal intensity within the lesioned CC area 1 and 7 d after stroke in vehicle-treated relative to sham-operated mice, which was greatly improved and restored by 3K3A-APC treatment 1 and 7 d after stroke, respectively, as indicated by 48% and only 12% lower values in MBP signal intensity compared with sham-operated controls (Fig. 3 D). The analysis of SMI 312 signal intensity (Fig. 3 E) confirmed a substantial loss of axonal density

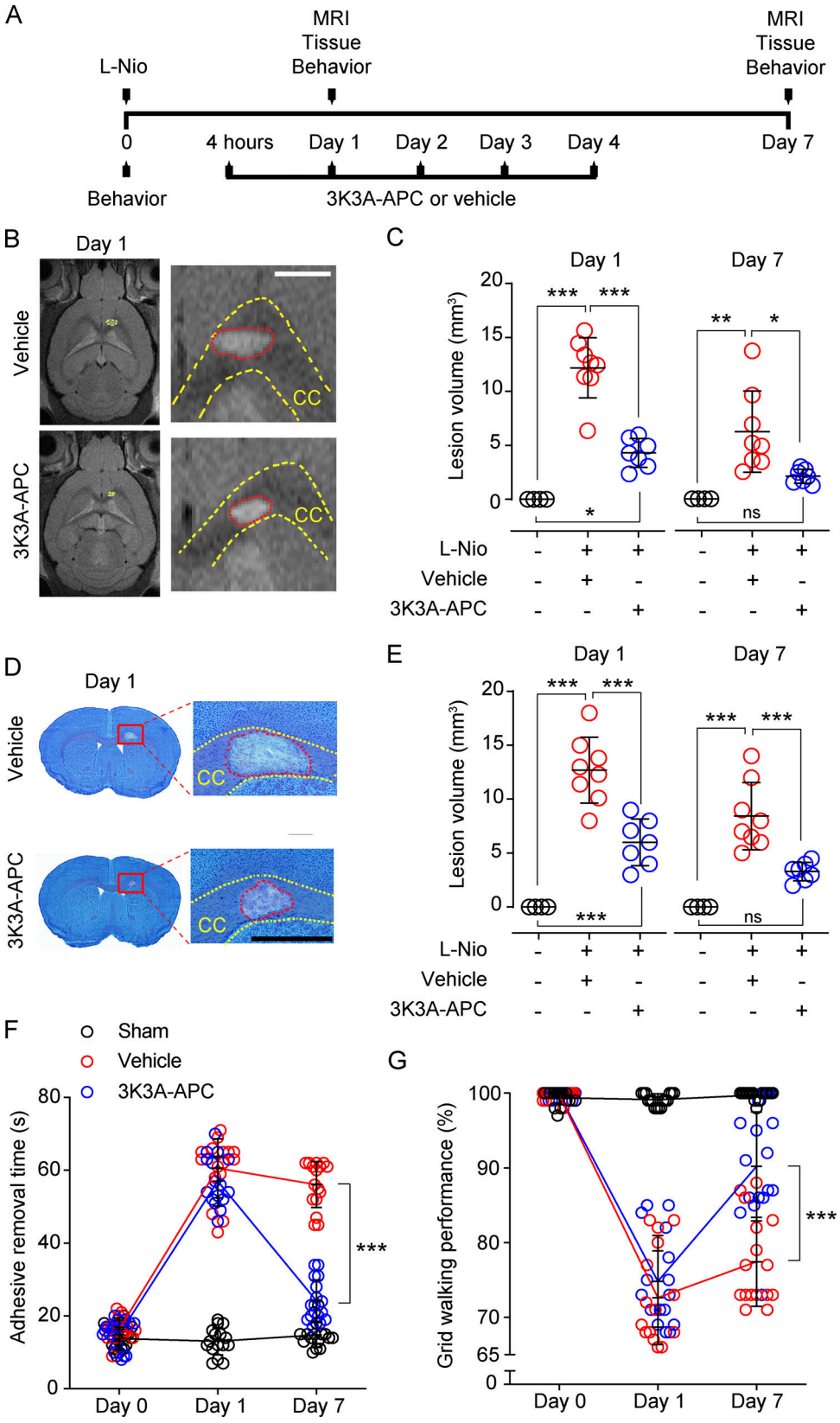

Figure 1. **3K3A-APC reduces lesion volume and improves functional outcome after WM stroke. (A)** Diagram of the experimental design. Mice received stereotaxic injections of L-Nio (3 × 40 nl, 30 mg/ml) into the CC and were treated with intravenous 3K3A-APC (0.2 mg/kg/d) or vehicle for 5 d. Control animals were sham-operated. MRI and tissue analyses were performed on days 1 and 7 after stroke. Behavioral tests were performed before stroke and on days 1 and 7 after stroke. **(B and C)** Representative T2-weighed MRI scans showing lesion volumes in the CC in vehicle-treated and 3K3A-APC–treated mice on day 1 after stroke (B; scale bar, 500 µm), and quantification of CC lesion volumes in vehicle-treated (red circles) and 3K3A-APC–treated (blue circles) mice on days 1 and 7

after stroke (C). Black circles, sham-operated mice. **(D and E)** Representative images of CC lesion volumes determined with the Cresyl Violet stain on coronal brain sections in vehicle-treated and 3K3A-APC–treated mice on day 1 after stroke (D; scale bar, 500 µm) and quantification of CC lesion volumes in vehicle-treated (red circles) and 3K3A-APC–treated (blue circles) mice on days 1 and 7 after stroke (E). Black circles, sham-operated mice. In C and E, mean ± SD, n = 7–8 mice per group for L-Nio stroke mice treated with vehicle or 3K3A-APC; n = 4 mice per group for sham-operated controls. **(F and G)** Adhesive removal (F) and grid-walking (G) tests in vehicle-treated (red circles) and 3K3A-APC–treated (blue circles) mice. Black circles, sham-operated mice. Mean ± SD, n = 16 mice per group. P values were calculated by one-way ANOVA followed by Bonferroni's multiple comparisons test. *, P < 0.05; **, P < 0.01; ***, P < 0.001.

by 83% and 73% on days 1 and 7 after stroke in vehicle-treated relative to sham-operated mice, which was greatly improved and restored by 3K3A-APC on days 1 and 7 after stroke, as shown by 47% and only 10% lower values compared with sham-operated controls, respectively (Fig. 3 F).

3K3A-APC protects oligodendrocytes from ischemic injury

Because 3K3A-APC ameliorated and/or prevented loss of myelin in the lesioned CC area on days 1 and 7 after stroke, respectively (Fig. 3, C and D), we next studied whether 3K3A-APC can protect oligodendrocytes, the myelinated cells of the central nervous system, from ischemic injury. Triple staining for Olig2 (oligodendrocyte transcription factor 2), cyclic nucleotide phosphodiesterase (CNPase, a marker for mature myelinating oligodendrocytes [OLs]; Baumann and Pham-Dinh, 2001; Montagne et al., 2018), and terminal deoxynucleotidyl transferase dUTP nick-end labeling (TUNEL) for DNA fragmentation suggestive of apoptotic and/or necrotic cell death (Figs. 4 A and S2 A) indicated increased numbers of dying Olig2$^+$CNPase$^+$TUNEL$^+$ OLs in the lesioned CC area in vehicle-treated compared with sham-operated mice on days 1 and 7 after stroke, which was substantially reduced by 3K3A-APC by 35% and 63%, respectively (Fig. 4 B). Consistent with these findings, we found 81% and 72% loss of Olig2$^+$CNPase$^+$ matured OLs in the lesion area in vehicle-treated compared with sham-operated mice on days 1 and 7 after stroke (Fig. 4 C). The Olig2$^+$CNPase$^+$ OL pool was protected by 3K3A-APC, as indicated by a less severe loss of 70% on day 1 after stroke, and only 10% loss relative to control values in sham-operated mice on day 7 after stroke, suggesting almost complete protection (Fig. 4 C).

Triple staining for Olig2, platelet-derived growth factor receptor α (PDGFRα, a marker for oligodendrocyte progenitor cells [OPCs]; Baumann and Pham-Dinh, 2001; Montagne et al., 2018), and TUNEL (Figs. 4 D and S2 B) indicated an increased number of Olig2$^+$PDGFRα$^+$TUNEL$^+$ OPCs in the lesioned CC area in vehicle-treated relative to sham-operated mice on days 1 and 7 after stroke, and this indicated significant reductions in the number of dying OPCs in mice treated with 3K3A-APC compared with vehicle by 31% and 58% on days 1 and 7 after stroke (Fig. 4 E). There was 80% and 75% loss of Olig2$^+$PDGFRα$^+$ OPCs in vehicle-treated compared with sham-operated mice on days 1 and 7 after stroke, which was greatly improved by 3K3A-APC with losses of 60% of Olig2$^+$PDGFRα$^+$ OPCs on day 1 and only 10% of Olig2$^+$PDGFRα$^+$ OPCs compared with sham-operated controls on day 7 after stroke, suggesting almost complete protection (Fig. 4 F). Additionally, MBP and TUNEL double staining in cultured primary mouse OLs subjected to oxygen and glucose deprivation (OGD), a model of ischemic injury in vitro (Montagne et al., 2018), showed that 3K3A-APC dose-dependently protected OLs from OGD-induced cell death, with half-maximal effective concentration (EC_{50}) of 5.5 nM (Fig. 4, G and H).

3K3A-APC suppresses microglia and astrocyte responses and expression of proinflammatory cytokines after WM stroke

As previously reported (Rosenzweig and Carmichael, 2013), we found a considerable increase in Iba1$^+$ (ionized calcium-binding adaptor protein 1) microglia around the lesioned CC area 1 d after stroke in vehicle-treated mice compared with sham controls (Fig. 5 A), which was almost completely suppressed by 3K3A-APC (Fig. 5 B), consistent with 3K3A-APC's anti-inflammatory activity (Griffin et al., 2015; Griffin et al., 2018) and suppression of microglia in models of ALS (Zhong et al., 2009) and AD (Lazic et al., 2019). Similarly, there was an increase in glial-fibrillar acidic protein (GFAP)-positive reactive astrocytes in the lesioned CC area 1 d after stroke (Fig. 5, C and D), as reported (Sozmen et al., 2019), which was completely suppressed by 3K3A-APC. Focal ischemic stroke leads to increased mRNA levels of proinflammatory cytokines and chemokines in the CC (Rosenzweig and Carmichael, 2013), as we confirmed here by showing increased mRNA levels for tumor necrosis factor α (*Tnf-α*), IL-6 (*Il-6*), IL-1β (*Il-1β*), and chemokine (C-C) motif ligand 2 (*Ccl-2*) on day 1 after stroke in vehicle-treated mice. In this study, we did not determine the exact cellular source of elevated cytokines and chemokines after WM stroke or whether they are produced primarily by microglia, astrocytes, and/or (more likely) by both cell types. However, 3K3A-APC completely reversed cytokine/chemokine changes back to control values seen in sham-operated control mice (Fig. 5 E).

3K3A-APC protects ischemic oligodendrocytes in vitro and in vivo via PAR1 and PAR3

In the search for APC receptors required for 3K3A-APC protection of OLs and OPCs and WM after ischemic injury, we focused on PARs known to mediate APC's beneficial cell-signaling effects (Griffin et al., 2015; Griffin et al., 2018). OLs and OPCs were freshly isolated from mouse WM by FACS using their cell-specific markers as shown in Fig. 6 A and as previously described (Montagne et al., 2018). *F2r* (encoding PAR1), *F2rl* (encoding PAR2), *F2rl2* (encoding PAR3), and *F2rl3* (encoding PAR4) mRNAs were all present in both OLs and OPCs (Fig. 6 B) and in primary mouse microglia, astrocytes, and neurons (Fig. 6 C). These results were confirmed by Western blotting for different PARs in OLs, microglia, astrocytes, and neuron cell lysates using PAR1–4-specific antibodies (Fig. 6 D), as reported (Lazic et al., 2019), with the exception of extremely low expression of PAR4 in microglia, astrocytes, and neurons (Fig. 6 D). OLs, microglia, astrocytes, and neurons were positive for their cell-specific markers Olig2, Iba1, GFAP, and β III tubulin,

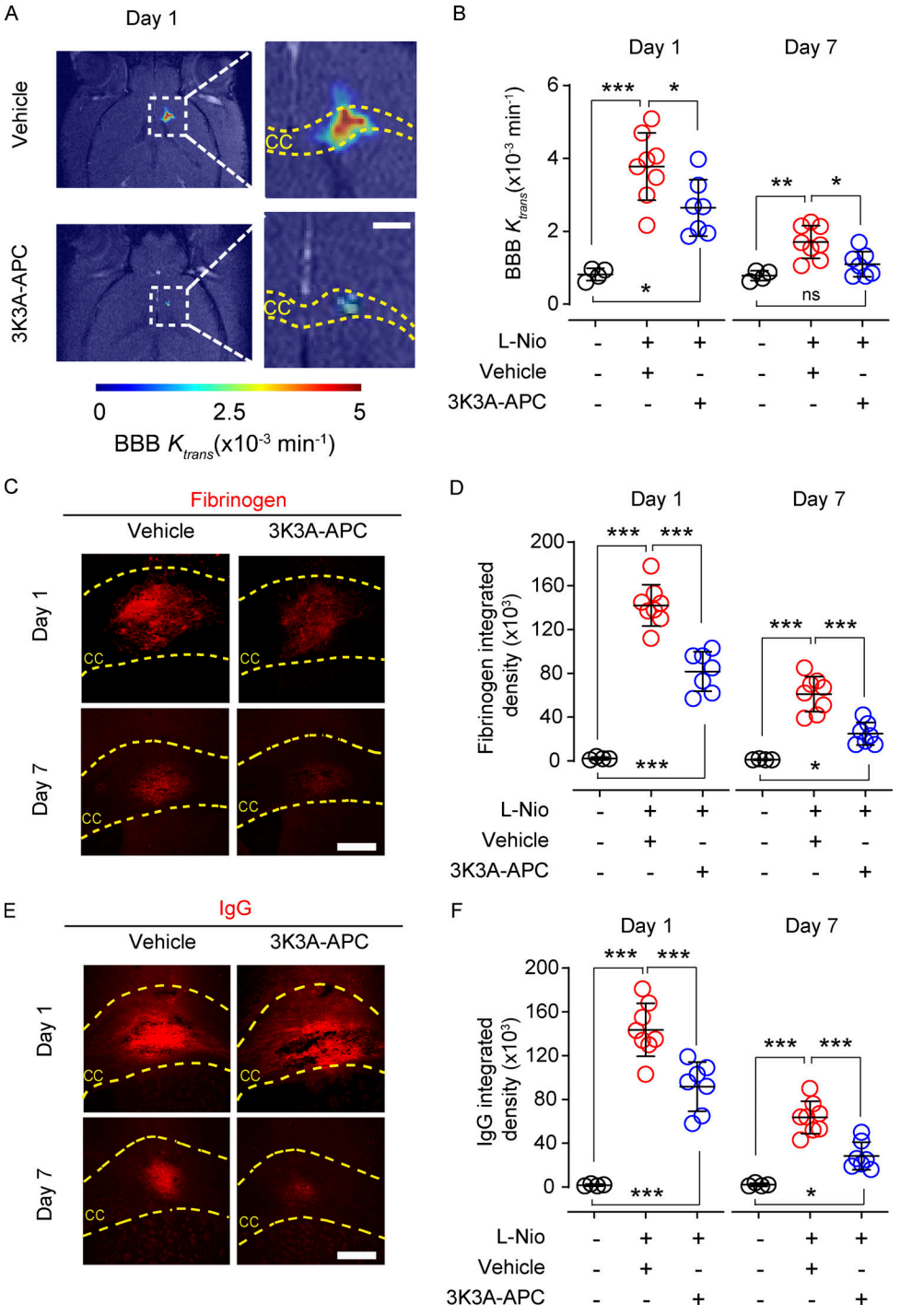

Figure 2. **3K3A-APC improves BBB integrity after WM stroke. (A and B)** Representative BBB permeability K_{trans} maps in the CC in vehicle-treated and 3K3A-APC–treated mice on day 1 after stroke, determined from DCE-MRI scans (A; scale bar, 500 µm), and BBB permeability constant K_{trans} values at the lesion site in vehicle-treated (red circles) and 3K3A-APC–treated (blue circles) mice on days 1 and 7 after stroke (B). Black circles, sham-operated mice. **(C–F)** Representative images of fibrinogen (C; scale bar, 200 µm) and IgG (E; scale bar, 200 µm) extravascular deposits in vehicle-treated and 3K3A-APC–treated mice on days 1 and 7 after stroke, and quantification of fibrinogen (D) and IgG (F) extravascular deposits in vehicle-treated (red circles) and 3K3A-APC–treated (blue circles) mice on days 1 and 7 after stroke. Black circles, sham-operated mice. In B, D, and F, mean ± SD, n = 7–8 mice per group for L-Nio stroke mice treated with vehicle or 3K3A-APC; n = 4 mice per group for sham-operated controls. P values were calculated by one-way ANOVA followed by Bonferroni's multiple comparisons test. *, P < 0.05; **, P < 0.01; ***, P < 0.001.

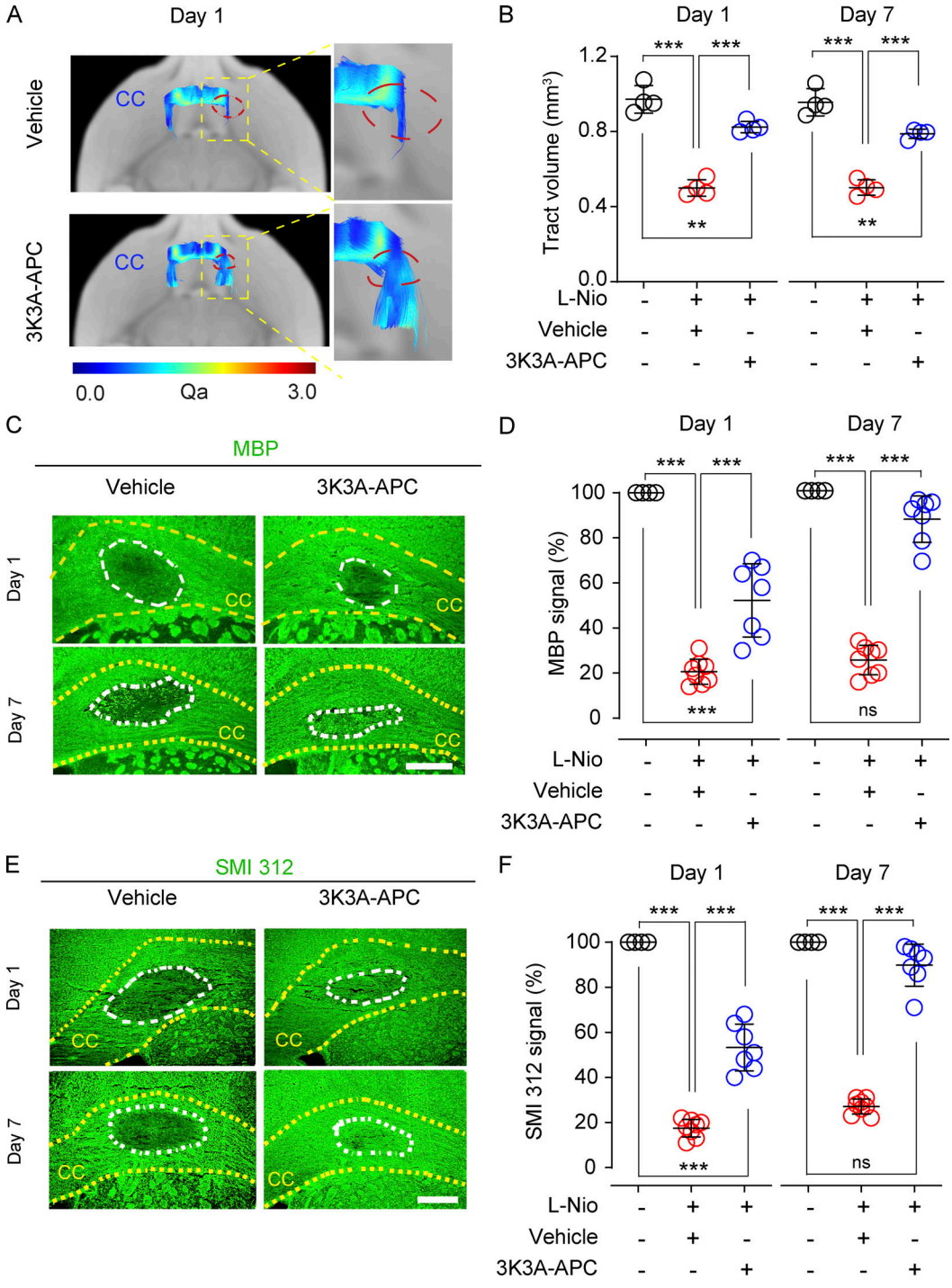

Figure 3. **3K3A-APC protects structural integrity of the WM tracts and prevents myelin loss after WM stroke. (A and B)** Representative 3D fiber tracking at the lesion site in the CC in vehicle-treated and 3K3A-APC–treated mice determined in vivo from DWI MRI (EPI-DTI) scans on day 1 after stroke (A), and quantification of CC tract volumes at the lesion site in vehicle-treated (red circles) and 3K3A-APC–treated (blue circles) mice on days 1 and 7 after stroke (B). Black circles, sham-operated mice; Qa, quantitative anisotropy measuring fiber density. Mean ± SD, *n* = 4 mice per group. **(C and D)** Immunostaining for MBP at the lesion site in the CC in vehicle-treated and 3K3A-APC–treated mice on days 1 and 7 after stroke (C; scale bar, 150 µm), and quantification of MBP signal intensity at the lesion site in vehicle-treated (red circles) and 3K3A-APC–treated (blue circles) mice on days 1 and 7 after stroke (D). Black circles, sham-operated mice. **(E and F)** Immunostaining for SMI 312 neuritic marker at the lesion site in the CC in vehicle-treated and 3K3A-APC–treated mice on days 1 and 7 after stroke (E; scale bar, 150 µm), and quantification of SMI 312 signal intensity at the lesion site in vehicle-treated (red circles) and 3K3A-APC–treated (blue circles) mice on days 1 and 7 after stroke (F). Black circles, sham-operated mice. In D and F, mean ± SD, *n* = 7–8 mice per group for L-Nio stroke mice treated with vehicle or 3K3A-APC; *n* = 4 mice per group for sham-operated controls. MBP and SMI 312 signal intensity in sham-operated controls were arbitrarily taken as 100%. P values were calculated by one-way ANOVA followed by Bonferroni's multiple comparisons test. **, P < 0.01; ***, P < 0.001.

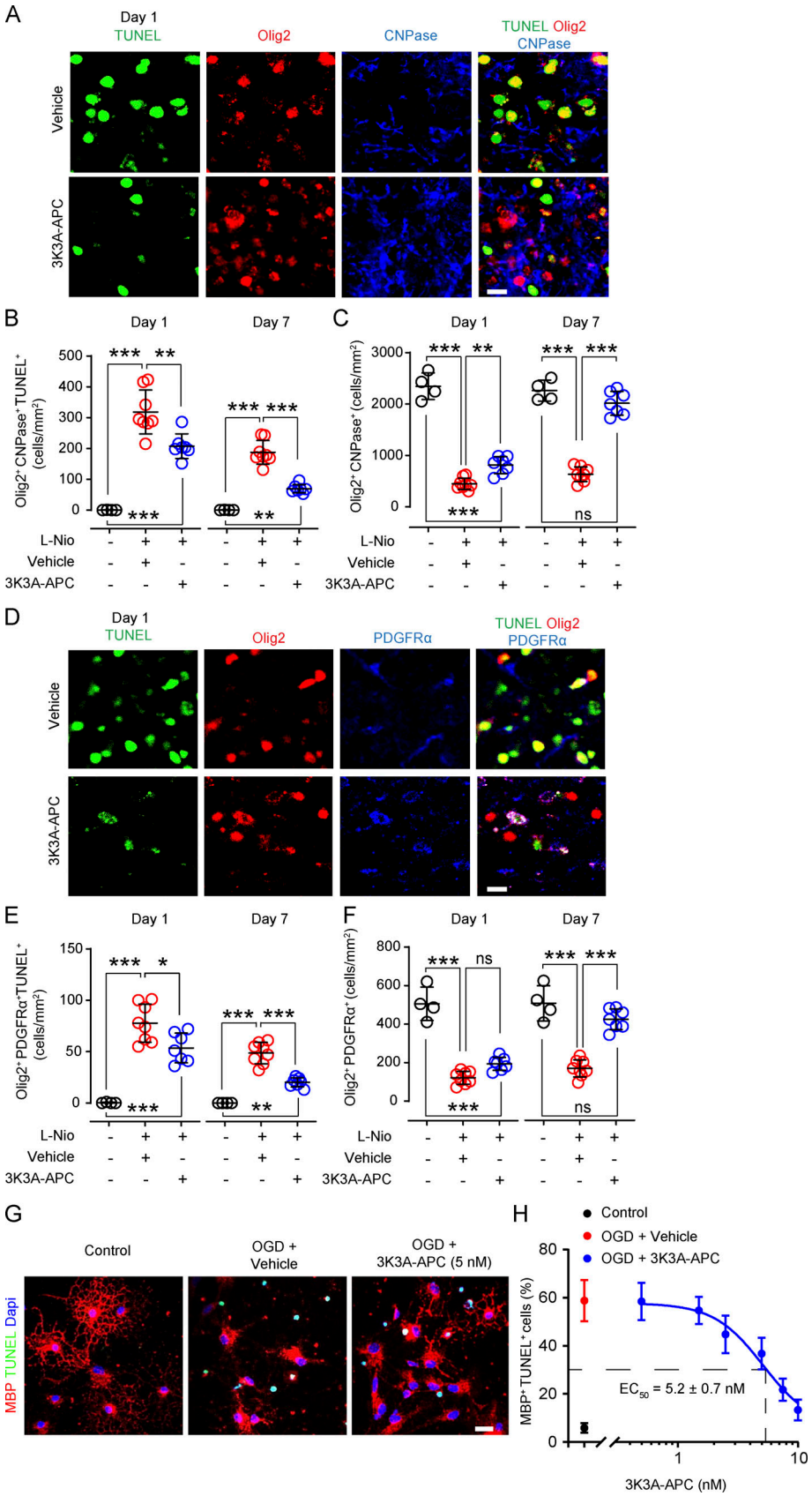

Figure 4. **3K3A-APC protects oligodendrocytes from ischemic injury in vivo and in vitro. (A–C)** Olig2, CNPase, and TUNEL staining at the lesion site in the CC in vehicle-treated and 3K3A-APC–treated mice on day 1 after stroke (A; scale bar, 20 µm), and quantification of Olig2$^+$CNPase$^+$TUNEL$^+$ triple-positive dying OLs (B) and Olig2$^+$CNPase$^+$ double-positive mature OLs (C) at the lesion site in vehicle-treated (red circles) and 3K3A-APC–treated (blue circles) mice on days

1 and 7 after stroke. Black circles, sham-operated mice. **(D–F)** Olig2, PDGFRα, and TUNEL staining at the lesion site in the CC in vehicle-treated and 3K3A-APC–treated mice on day 1 after stroke (D; scale bar, 20 µm), and quantification of Olig2$^+$ PDGFRα$^+$TUNEL$^+$ triple-positive dying OPCs (E) and Olig2$^+$PDGFRα$^+$ double-positive OPCs (F) at the lesion site in vehicle-treated (red circles) and 3K3A-APC–treated (blue circles) mice on days 1 and 7 after stroke. Black circles, sham-operated mice. In B, C, E, and F, mean ± SD, *n* = 7–8 mice per group for L-Nio stroke mice treated with vehicle or 3K3A-APC; *n* = 4 mice per group for sham-operated controls. **(G)** MBP$^+$ and TUNEL$^+$ double-positive primary mouse OLs cultures subjected to OGD or vehicle for 6 h (scale bar, 20 µm) and treated with vehicle or 3K3A-APC (5 nM). **(H)** Quantification of MBP$^+$TUNEL$^+$ OLs subjected to OGD for 6 h and treated with vehicle or 3K3A-APC (0.5–10 nM). Mean ± SD from three independent cultures (each with five coverslips averaged per experiment). P values were calculated by one-way ANOVA followed by Bonferroni's multiple comparisons test. *, P < 0.05; **, P < 0.01; ***, P < 0.001.

respectively, and negative for other studied cellular markers (not depicted).

Next, we challenged primary mouse OLs with OGD (Montagne et al., 2018) and used live/dead assays to study the effects of 3K3A-APC in OLs with PAR1, PAR2, PAR3, and/or PAR4 being silenced by the respective siRNAs, as previously reported (Lazic et al., 2019). The results were compared with findings in OLs transfected with si.Control. Our data show that silencing PAR1 and PAR3 with si*F2r* and si*F2rl2*, respectively, but not PAR2 or PAR4 with si*F2rl1* and si*F2rl3*, resulted in loss of

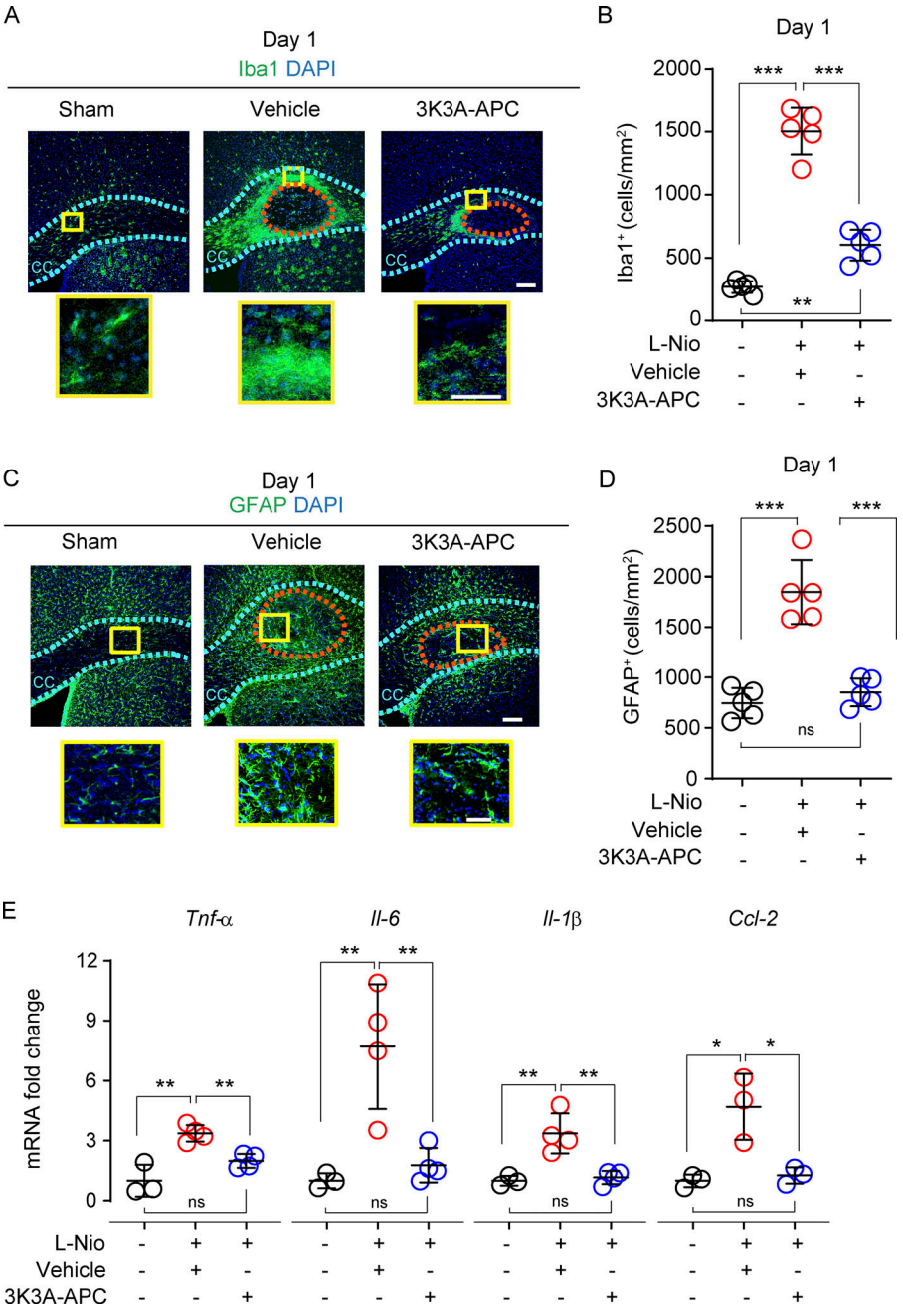

Figure 5. **3K3A-APC suppresses microglia and astrocyte responses and production of cytokines after WM stroke. (A and B)** Immunostaining for Iba1$^+$ microglia in the perilesion area in the CC in vehicle-treated and 3K3A-APC–treated mice on day 1 after stroke (A; scale bar, 100 µm), and quantification of Iba1$^+$ microglia in the perilesion site in vehicle-treated (red circles) and 3K3A-APC–treated (blue circles) mice on day 1 after stroke (B). Black circles, sham-operated mice. **(C and D)** Immunostaining for GFAP$^+$ astrocytes at the lesion site in the CC in vehicle-treated and 3K3A-APC–treated mice on day 1 after stroke (C; scale bar, 100 µm), and quantification of GFAP$^+$ astrocytes at the lesion site in vehicle-treated (red circles) and 3K3A-APC–treated (blue circles) mice on day 1 after stroke (D). Black circles, sham-operated mice. In B and D, mean ± SD, *n* = 5 mice/group. Boxes in A and C denote sites taken for higher-magnification insets shown below main images (scale bar, 50 µm). **(E)** Relative abundance of *Tnf-α*, *Il-6*, *Il-1β*, and *Ccl-2* mRNA levels normalized to the housekeeping *Gapdh* gene at the lesion site in vehicle-treated (red circles) and 3K3A-APC–treated (blue circles) mice on day 1 after stroke. Mean ± SD, *n* = 3–4 mice per group. Black circles, sham-operated mice. P values were calculated by one-way ANOVA followed by Bonferroni's multiple comparisons test. *, P < 0.05; **, P < 0.01; ***, P < 0.001.

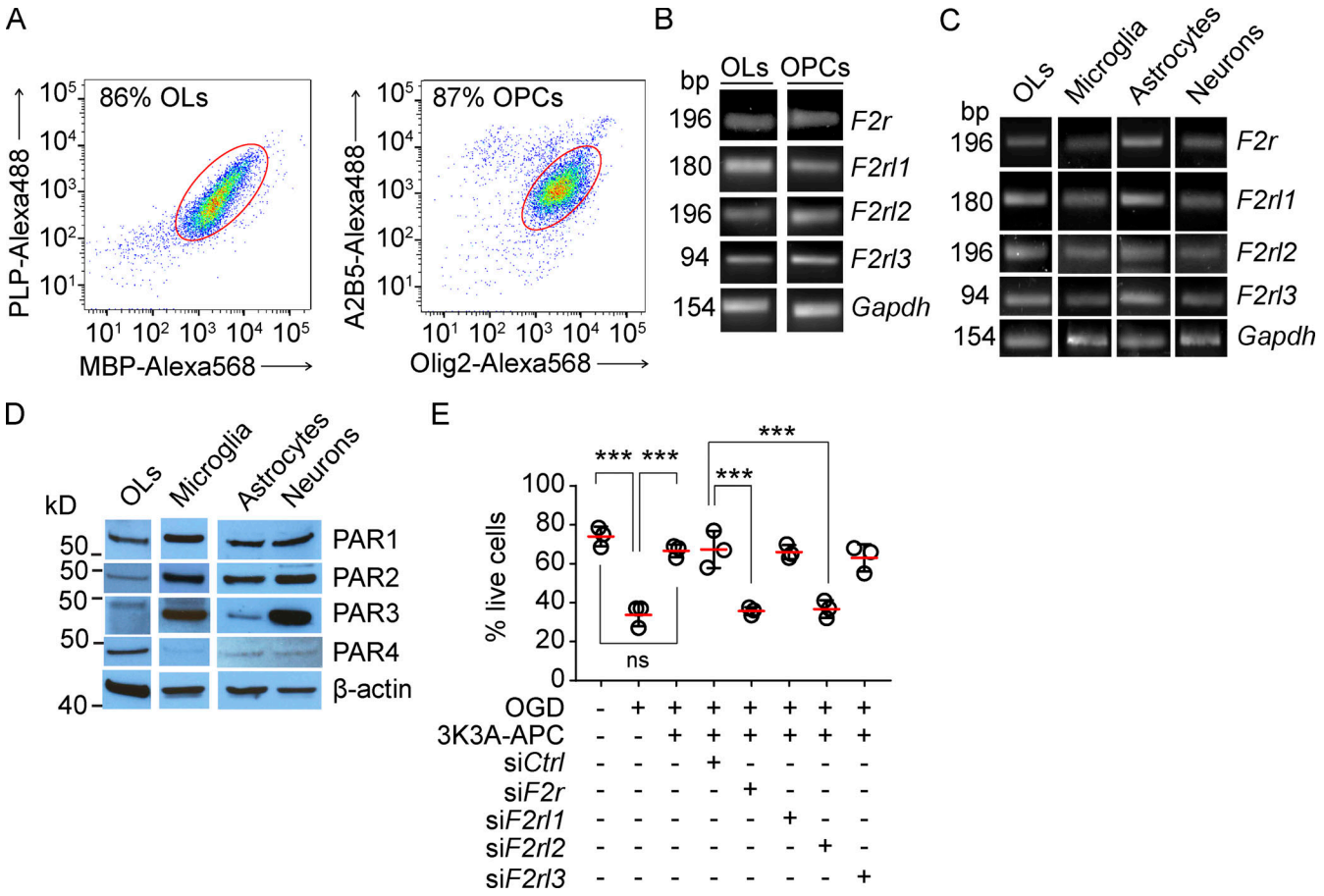

Figure 6. **Expression of PAR1-4 in oligodendrocytes, microglia, and astrocytes, and 3K3A-APC protection of ischemic oligodendrocytes in vitro via PAR1 and PAR3. (A)** Representative dot plots of the flow cytometry analysis of MBP-Alexa Fluor 568⁺ and proteolipid protein–Alexa Fluor 488⁺ OLs (left) and A2B5-Alexa Fluor 568⁺ and Olig2-Alexa Fluor 488⁺ OPCs (right) freshly isolated from mouse WM. **(B and C)** RT-qPCR for *F2r* (encodes PAR1), *F2rl* (encodes PAR2), *F2rl2* (encodes PAR3), and *F2rl3* (encodes PAR4) in WM mouse OLs and OPCs (B) and in OLs and primary mouse microglia, astrocyte, and neuron cultures (B). *Gapdh*, housekeeping gene. **(D)** Immunoblotting for PAR1, PAR2, PAR3, and PAR4 in mouse OLs and microglia, astrocyte, and neuron cell lysates. **(E)** OL cultures with silenced PAR1, PAR2, PAR3, or PAR4 with si*F2r*, si*F2rl1*, si*F2rl2*, and si*F2rl3*, respectively, were subjected to OGD and treated with 3K3A-APC (5 nM) or vehicle at 7 d in vitro. si*Ctrl* served as a control. The viability of OLs was assessed with live/dead assay 6 h after OGD. Mean ± SD from three independent experiments (each with five coverslips averaged per experiment). P values were calculated by one-way ANOVA followed by Bonferroni's multiple comparisons test. ***, P < 0.001. Representative dot plots (A), gels (B and C), and Western blots (D) are from two independent experiments each.

3K3A-APC's protection of OGD-treated OLs, indicating that PAR1 and PAR3 are required for 3K3A-APC protection of OLs from ischemic insult in vitro (Fig. 6 E).

We then went back to our WM stroke model to determine whether PAR1 and PAR3 were also required for 3K3A-APC–mediated protection of the WM and oligodendrocytes in vivo. To silence PAR1 and PAR3, *F2r* siRNA or *F2rl2* siRNAs, and/or si.Control, were administered intracerebroventricularly (ICV) bilaterally, as we previously reported for in vivo silencing of genes expressed by different brain cell types (Montagne et al., 2018; Nikolakopoulou et al., 2019). First, we showed that ICV administration of *F2r* siRNA and *F2rl2* siRNAs almost completely silenced PAR1 and PAR3 in the CC WM lysates, respectively, 1 wk after transfection (Fig. 7 A). After challenging mice with focal WM stroke, we found that the lesion volumes on day 1 after stroke in 3K3A-APC–treated mice with either silenced PAR1 or PAR3 were comparable to those in vehicle-treated mice (Fig. 7, B and C), suggesting loss of protection. The lesion volumes, however, were not affected by PAR1 or PAR3 silencing in vehicle-treated mice (Fig. 7 C).

Consistent with these findings, PAR1 or PAR3 silencing led to loss of 3K3A-APC protection of OLs and OPCs, as shown by numbers of Olig2⁺CNPase⁺TUNEL⁺ mature OLs (Fig. 7, D and E; and Fig. S3 A) and Olig2⁺ PDGFRα⁺TUNEL⁺ OPCs (Fig. 7, F and G; and Fig. S3 B) at the lesion site 1 d after stroke, which were comparable to the respective numbers in vehicle-treated mice. PAR1 or PAR3 silencing did not have an effect on numbers of Olig2⁺CNPase⁺TUNEL⁺ mature OLs or OPCs in vehicle-treated control mice (Fig. 7, E and G).

3K3A-APC requires PAR1 and PAR3 to suppress microglia and astrocyte responses after WM stroke

PAR1 or PAR3 silencing in vivo, as described above, also led to loss of 3K3A-APC's suppression of both microglia responses (Fig. 8, A and B; and Fig. S3 C) and astrocyte responses (Fig. 8, C and D; and Fig. S3 D). PAR1 or PAR3 silencing did not affect the

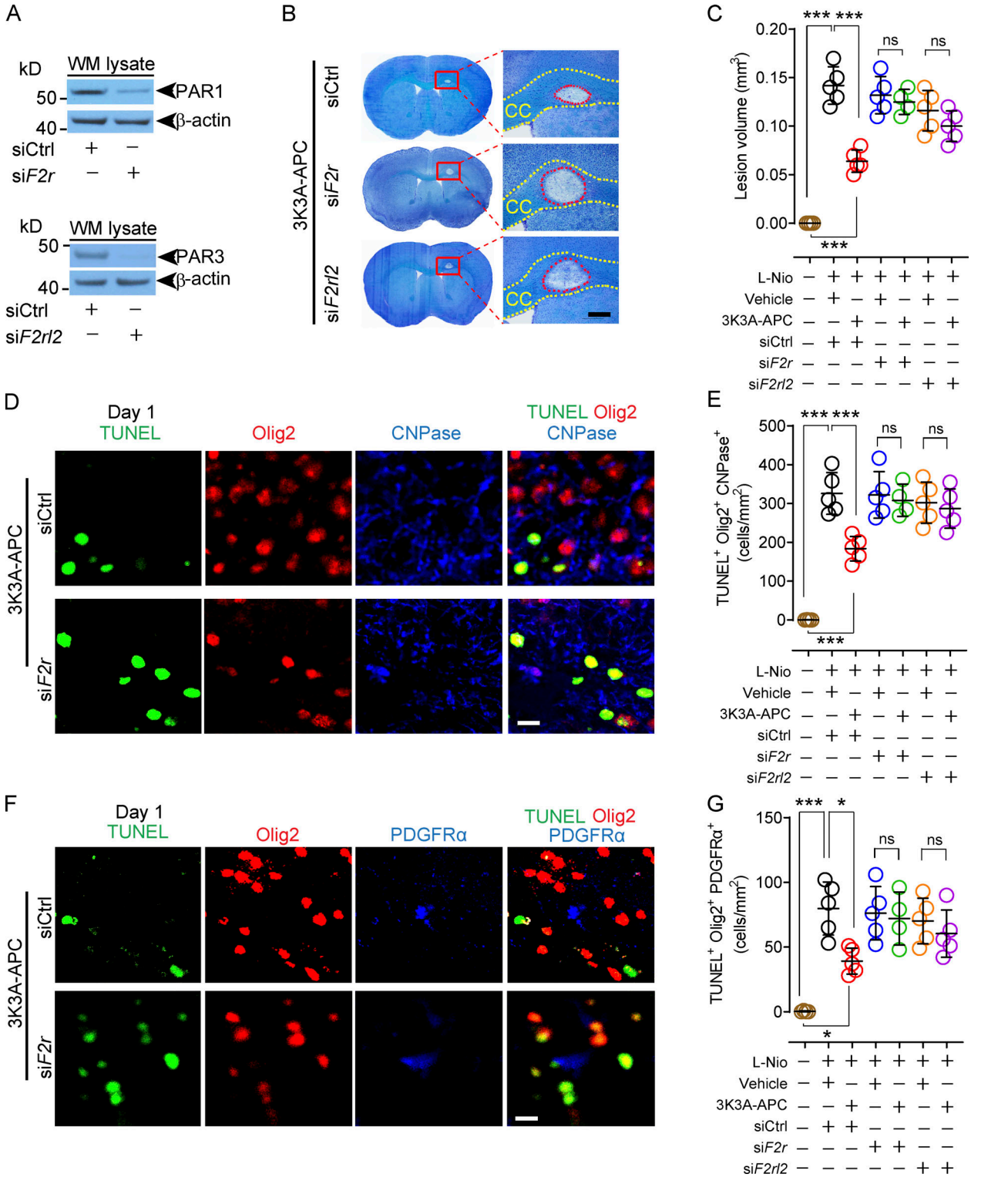

Figure 7. **PAR1 and PAR3 silencing abolishes 3K3A-APC's protection of oligodendrocytes after WM stroke. (A)** Immunoblotting for PAR1 and PAR3 in the WM lysates pooled from three mice after PAR1 and PAR3 silencing by ICV delivery of si*F2r* and si*F2rl2*, respectively, or si*Ctrl*. **(B and C)** Cresyl Violet stain of coronal brain sections after PAR1 and PAR3 silencing compared with si*Ctrl* on day 1 after stroke (B; scale bar, 100 µm), and quantification of the lesion volume in the CC after PAR1 (green circles) and PAR3 (purple circles) silencing in 3K3A-APC–treated mice compared with siCtrl (red circles), and in vehicle-treated mice after siCtrl (black circles), PAR1 (blue circles), and PAR3 (orange circles) silencing on day 1 after stroke (C). Brown circles, sham-operated controls. **(D and E)** Olig2, CNPase, and TUNEL staining for dying OLs at the CC lesion site in 3K3A-APC–treated mice after silencing PAR1 compared with si*Ctrl* on day 1 after stroke (D; scale bar, 20 µm), and quantification of $Olig2^+CNPase^+TUNEL^+$ dying OLs in 3K3A-APC–treated mice after silencing PAR1 (green circles) and PAR3 (purple circles) compared with siCtrl (red circles), and in vehicle-treated mice after siCtrl (black circles), PAR1 (blue circles), and PAR3 (orange circles) silencing on day 1 after stroke (E). Brown circles, sham-operated controls. **(F and G)** Olig2, PDGFRα, and TUNEL staining at the CC lesion site for dying OPCs in

3K3A-APC–treated mice after PAR1 silencing compared with si*Ctrl* on day 1 after stroke (F; scale bar, 20 µm), and quantification of Olig2⁺PDGFRα⁺TUNEL⁺ dying OPCs in 3K3A-APC–treated mice after PAR1 (green circles) and PAR3 (purple circles) silencing compared with siCtrl (red circles), and in vehicle-treated mice after siCtrl (black circles), PAR1 (blue circles), and PAR3 (orange circles) silencing on day 1 after stroke (G). Brown circles, sham-operated controls. In C, E, and G, mean ± SD, *n* = 4–5 mice per group. P values were calculated by one-way ANOVA followed by Bonferroni's multiple comparisons test. Representative Western blots (A) are from two independent experiments each. *, P < 0.05; ***, P < 0.001.

numbers of Iba1⁺ microglia and GFAP⁺ astrocytes in vehicle-treated control mice (Fig. 8, B and D).

Discussion

Using multiparametric MRI, high-resolution confocal microscopy tissue analysis, and biochemical assays as previously described (Montagne et al., 2018; Nikolakopoulou et al., 2019), we show here that 3K3A-APC protects the WM tracts and oligodendrocytes from ischemic injury in middle-aged mice and that it suppresses microglia and astrocyte responses and proinflammatory cytokine and chemokine production, consequently reducing lesion volume in the CC and improving post–WM stroke sensory-motor and motor functions. Since the cell numbers in each mouse quantification analysis have been normalized per square millimeter within the lesion area for OLs, OPCs, and astrocytes, or within the well-defined perilesion area around the edge of the infarct for microglia (see Materials and methods), the reduced numbers of TUNEL⁺ OLs, TUNEL⁺ OPCs, Iba1⁺ microglia, and GFAP⁺ astrocytes reflect 3K3A-APC's direct post–WM stroke effects on different cell types in the WM, rather than reflecting the difference in the injury size.

Using siRNAs to silence various PARs, we showed that that 3K3A-APC beneficial effects after WM stroke required PAR1 and PAR3. At the cellular level, this has been shown in OL cultures, when silencing PAR1 and PAR3, but not PAR2 and PAR4, led to protection against ischemic insult in vitro, which was confirmed in vivo for both OLs and OPCs after WM stroke. These data provide the first mechanistic findings showing that the APC pathway is active in OLs. Data also show that both OLs and OPCs freshly isolated from the WM express all four PAR receptors. Recent single-cell RNA sequencing studies focused mainly on vascular transcriptome and/or different subpopulations of neurons found to have *F2r* expression (encoding PAR1) in mouse

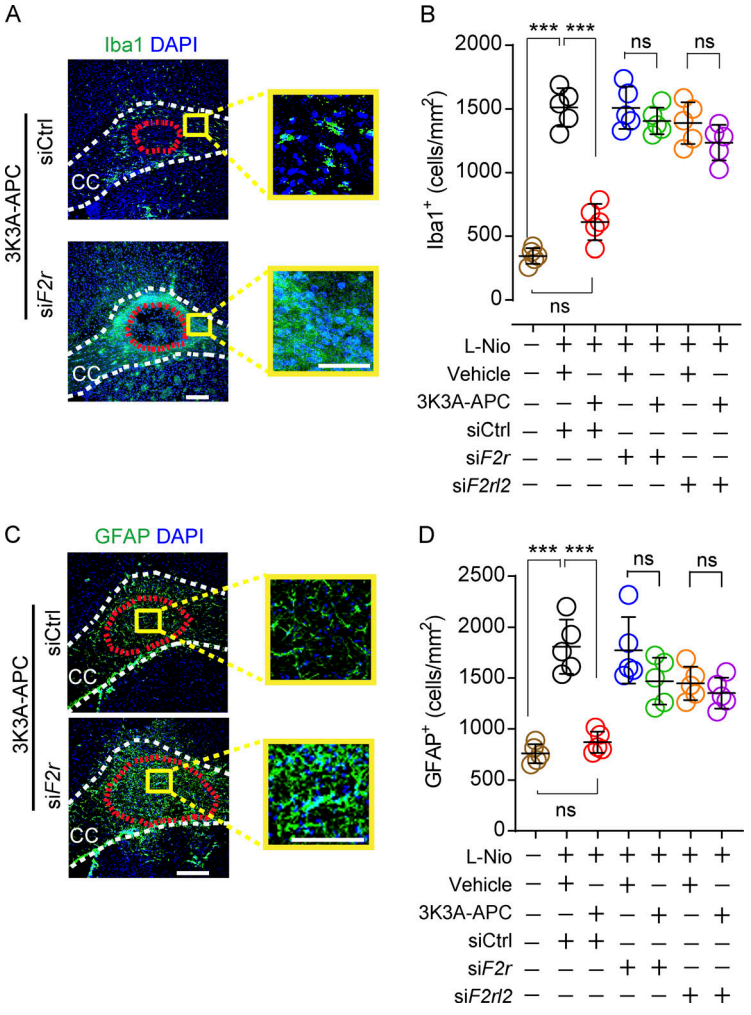

Figure 8. **PAR1 and PAR3 silencing abolishes 3K3A-APC's suppression of microglia and astrocyte responses after WM stroke. (A and B)** Immunostaining for Iba1⁺ microglia in the perilesion area in the CC in 3K3A-APC–treated mice after PAR1 silencing compared with si*Ctrl* on day 1 after stroke (A; scale bar, 100 µm), and quantification of Iba1⁺ microglia in the prelesion site in 3K3A-APC–treated mice after PAR1 (green circles) and PAR3 (purple circles) silencing compared with siCtrl (red circles), and in vehicle-treated mice after siCtrl (black circles), PAR1 (blue circles), and PAR3 (orange circles) silencing on day 1 after stroke (B). Brown circles, sham-operated controls. **(C and D)** Immunostaining for GFAP⁺ astrocytes at the CC lesion site in 3K3A-APC–treated mice after silencing PAR1 compared with si*Ctrl* on day 1 after stroke (C; scale bar, 100 µm), and quantification of GFAP⁺ astrocytes at the lesion site in 3K3A-APC–treated mice after PAR1 (green circles) and PAR3 (purple circles) silencing compared with siCtrl (red circles), and in vehicle-treated mice after siCtrl (black circles), PAR1 (blue circles), and PAR3 (orange circles) silencing on day 1 after stroke (D). Brown circles, sham-operated controls. Boxes in A and C denote sites taken for higher-magnification insets shown on a side of main images (scale bar, 50 µm). In B and D, mean ± SD, *n* = 4–5 mice per group. P values were calculated by one-way ANOVA followed by Bonferroni's multiple comparisons test. ***, P < 0.001.

OLs, but they were less conclusive regarding expression of other PARs (Vanlandewijck et al., 2018; Zeisel et al., 2018; Zeisel et al., 2015; Zhang et al., 2014). Other studies using RT-PCR of OL cultures and immunostaining of brain tissue sections showed that OLs express PAR1, PAR3, and PAR4 (Wang et al., 2004; Yoon et al., 2015), consistent with our findings showing that OLs and OPCs freshly isolated from WM express all four PARs. Thus, our data identify a novel pathway that protection of ischemic oligodendrocytes by 3K3A-APC requires PAR1 and PAR3. These findings suggest that both OLs and OPCs have similar requirements for PAR1 and PAR3 as known for APC's and 3K3A-APC's protection for neurons (Guo et al., 2004; Guo et al., 2009a; Guo et al., 2009b; Sinha et al., 2018) and neuronal progenitor cells (Guo et al., 2013; Wang et al., 2016b).

Although PAR3 was expressed in somewhat lower levels in OLs compared with neurons and microglia, the level of expression of PAR3 in a particular cell type is not a useful indication of its potential relevance. Namely, PAR1 can form heterodimers with PAR3 (McLaughlin et al., 2007), and APC may signal especially well when activating both PAR1 and PAR3 in their heterodimer. PAR1 is distributed, in part, on cell surface caveolae where EPCR is located, which is required for binding APC for EPCR-dependent PAR1 signaling (Russo et al., 2009). Therefore, it is speculated that 3K3A-APC's beneficial signaling employs the PAR1:PAR3 heterodimer in caveolae.

Previous studies have shown that 3K3A-APC suppresses microglia and astrocytes in ALS (Zhong et al., 2009) and AD (Lazic et al., 2019) models, but the mechanisms behind it, including the receptors involved, remain elusive. Here, we found that both PAR1 and PAR3 are required for 3K3A-APC's suppression of microglia and astrocytes' responses after WM stroke. Interestingly, expression of PAR1 and PAR3 in microglia increases after focal ischemia in rodents (Henrich-Noack et al., 2006), which could potentially facilitate 3K3A-APC or endogenous APC suppressive effects. Since inflammation is an important pathway in vascular dementia and WM damage, our results suggest that "gliosis" in both microglia and astrocytes may be dampened by 3K3A-APC. However, both microglia and astrocytes may show biphasic phenotypes—deleterious as well as beneficial—M1 versus M2 (Hu et al., 2012) and A1 versus A2 (Chan et al., 2019). Therefore, future studies should address if there is a delayed response of microglia and astrocytes due to 3K3A-APC treatment at later time points after WM stroke. Similarly, OPCs and OLs can suffer delayed apoptosis, and OPCs can differentiate into astrocytes at later points after WM stroke (Sozmen et al., 2016). Again, future studies should concentrate on elucidating whether 3K3A-APC can influence these late cellular events, as well as whether it can induce greater migration of OPCs from adjunct healthy tissue or higher proliferation of OPCs in addition to directly protecting OLs and OPCs from cell death, as shown here by TUNEL staining.

Protection of BBB integrity by 3K3A-APC after WM stroke reduced the level of toxic fibrinogen deposits in the WM and was consistent with protection of endothelial barrier dysfunction in different in vivo and in vitro models with APC and/or 3K3A-APC (Griffin et al., 2016; Griffin et al., 2015; Griffin et al., 2018; Lin et al., 2020). Previous work in pericyte-deficient mice has shown that fibrinogen can activate autophagy-dependent cell death of oligodendrocytes in the WM (Montagne et al., 2018). Whether fibrinogen can play a causal role in WM stroke is not clear at present but should be addressed by future studies in fibrinogen-deficient mice, as reported (Montagne et al., 2018). Previous studies suggested that receptors other than PAR1 such as Tie2 (Minhas et al., 2017), apoER2 (Sinha et al., 2016) and EPCR (Cheng et al., 2003; Griffin et al., 2018; Guo et al., 2009a; Guo et al., 2009b) also may play a role in protecting endothelium, and that the integrin Mac-1 (Cao et al., 2010) contributes to APC's protection against endotoxemia. Whether these receptors can play a role in the observed 3K3A-APC protection of endothelium in the WM is not clear at present and merits future additional studies.

Activation of PAR1 by APC and its signaling-selective analogues, e.g., 3K3A-APC, involves cleavage of PAR1 N-terminal domain at Arg46, which reveals a tethered ligand peptide that begins at Asn47 (P1–47), causing APC's biased, β-arrestin–dependent cytoprotective signaling (Mosnier et al., 2012; Schuepbach et al., 2012; Sinha et al., 2018; Soh and Trejo, 2011). In contrast, activation of PAR1 by thrombin involves cleavage at Arg41, which generates thrombin receptor–activated peptide, a tethered ligand initiating cytotoxic effects via G-protein–dependent signaling, causing human platelet activation, inflammatory changes, vascular leakage, and central nervous system toxicity (Mosnier et al., 2012). Similarly, APC activates human PAR3 by noncanonical cleavage at Arg41, whereas thrombin cleaves PAR3 at Lys38 (Burnier and Mosnier, 2013). PAR3-tethered ligand peptides beginning at amino acid 42, but not those beginning at amino acid 39, exert cytoprotective effects (Burnier and Mosnier, 2013; Stavenuiter and Mosnier, 2014), suggesting that human PAR3 cleavage at Arg41 initiates APC-like cytoprotection, whereas PAR3 cleavage at Lys38 initiates thrombin-like cytotoxic proinflammatory effects (Burnier and Mosnier, 2013). The role of PAR1 and PAR3 cleavage requirement sites and of β-arrestin cytoprotective signaling in 3K3A-APC protection against ischemic WM injury remains an important direction for future studies, not only from the mechanistic point of view but also because PAR1- and PAR3-derived peptides hold significant potential as prospective therapeutic APC-mimetic agents.

In humans, WM stroke progresses through expansion into the adjacent and damaged WM. This has yet to be reproduced in an experimental WM stroke model. Whether the length of assessment of the treatment measures can be extended beyond 7 d of WM stroke remains to be seen. For example, 15-mo-old mice at an age comparable to mice we used (12–15 mo old) show at 28 d of WM stroke a substantial spontaneous improvement in behavior, such as the grid walking task, leaving the window of 10% difference compared with sham controls (Rosenzweig and Carmichael, 2013). Such a narrow window would make it difficult for any treatment effect to be analyzed at 28 d. In contrast, vehicle-treated middle-aged mice did not show spontaneous recovery in behavior and or recovery of axonal/myelin integrity 7 d after stroke, the time point when 3K3A-APC completely normalized behavior and axonal/myelin integrity back to control values. This together with postischemic protection of OLs

and OPCs by 3K3A-APC suggest its cellular and tissue protective effects rather than acceleration of spontaneous tissue repair. Whether studies in 24-mo-old mice that show slower spontaneous recovery in behavior 28 d after WM stroke, with a margin of 15–20% difference compared with sham controls (Rosenzweig and Carmichael, 2013), will generate new mechanistic data regarding 3K3A-APC neuroprotection of the WM remains to be seen. The assessment of treatment in these aged mice, however, may be complicated by the interfering OPC differentiation into astrocytes occurring ∼10 d after WM stroke in old mice, as previously shown (Sozmen et al., 2019).

It is noteworthy that in contrast to L-Nio, injections of vehicle into the CC did not result in a detectable lesion in the CC on day 1 or 7 after injection, which rules out the possibility that the animals were under the effects of original surgery for 1 wk and/or that the effects of surgery contributed to behavioral deficits observed in vehicle-treated mice.

In light of the present findings and the considerable translational potential of the APC pathway (Lyden et al., 2013; Lyden et al., 2019; Williams et al., 2012), the most fitting indications for 3K3A-APC treatment would be ischemic stroke in patients who, in addition to gray-matter injury, develop the WM injury, which is the majority of stroke patients (Matute et al., 2013; Wang et al., 2016a; Feigin et al., 2018; Marin and Carmichael, 2018), as well as stroke in small brain vessels in subcortical WM regions, which is the second leading cause of dementia (Bos et al., 2018; Iadecola and Gottesman, 2018; Wardlaw et al., 2019; Wardlaw et al., 2015). Small lacunar subcortical strokes caused by small-vessel disease due to hypertension, diabetes, and other vascular risk factors, including hyperlipidemia and hyperhomocysteinemia, tend to be symptomatic (Wardlaw et al., 2019), and as such would be an excellent potential indication for 3K3A-APC.

3K3A-APC could also be used as a prevention therapy in humans diagnosed with diffuse WM ischemic lesions that develop silently over longer periods of time and are a major cause of human disability, including cognitive dysfunction (Iadecola and Gottesman, 2018; Wardlaw et al., 2019). The goal here would be to slow down progression and spreading of the WM lesions caused by recurrent WM strokes and/or reverse the process by administering a long-term 3K3A-APC therapy. Although we do not know whether long-term drug administration would be safe in humans, studies in animal models of ALS (Shi et al., 2019; Winkler et al., 2014; Zhong et al., 2009) and AD (Lazic et al., 2019) have shown that long-term daily treatments have been very beneficial, with no toxic side effects and normal liver and kidney function. Additionally, safety and pharmacokinetic studies in good laboratory practice toxicology in CD-1 mice and cynomolgus monkeys showed that a 14-d daily i.v. administration of 3K3A-APC at an increasing dose regimen, using the same route of administration as in humans, was safe and did not show signs of toxicity at any time (Williams et al., 2012).

In conclusion, the present study provides new insights into the functional neuroprotective APC pathway in the WM and identifies PAR1 and PAR3 as the receptors responsible for 3K3A-APC's protection of oligodendrocytes and suppression of microglia and astrocyte responses after ischemic insult in the WM. In addition to addressing new mechanistic questions related to PAR1 and PAR3 cleavage requirement sites and the role of β-arrestin's cytoprotective signaling functions, future studies should explore the efficacy of 3K3A-APC and the role of PAR1 and PAR3 APC-mimetic peptides (Healy et al., 2021) in other small-vessel disease models, such as pericyte-deficient mice (Montagne et al., 2018; Nikolakopoulou et al., 2019), endothelial nitric oxide–deficient mice (Liao et al., 2021), bilateral carotid artery stenosis (Liu et al., 2019), and/or cerebral autosomal dominant arteriopathy with subcortical infracts and leukoencephalopathy, a monogenic small-vessel disease causing vascular dementia (Ghosh et al., 2015).

Materials and methods

Animals

All procedures were approved by the Institutional Animal Care and Use Committee at the University of Southern California with National Institutes of Health guidelines. Middle-aged (12–15-mo-old) male C57BL/6J mice obtained from The Jackson Laboratory (000664) were used in this study. We used male mice to reduce sex bias. Of note, it has been shown that 3K3A-APC also protects aged female mice from embolic stroke (Wang et al., 2013). Future studies should reproduce the present findings in middle-aged or old female mice. Animals were randomized into treatment groups using GraphPad QuickCalcs (https://www.graphpad.com/quickcalcs/). All experiments were blinded; the operators responsible for experimental procedure and data analysis were blinded and unaware of group allocation throughout the experiment. Three mice were excluded from analysis: one based on lack of lesion on MRI, one died during surgery, and one had infection in the injection site.

3K3A-APC

Murine recombinant 3K3A-APC (KKK192-194AAA) was prepared in the Griffin laboratory as described previously (Mosnier et al., 2004).

WM stroke

WM stroke was produced by stereotaxic injections of L-Nio (30 mg/ml; Millipore) into the CC, as previously described (Rosenzweig and Carmichael, 2013; Sozmen et al., 2019; Sozmen et al., 2009; Sozmen et al., 2016). Three injections (40 nl) of L-Nio or vehicle were made using a micropipette and the Neurostar motorized ultraprecise small animal stereotaxic instrument (model 963SD) with the following coordinates: anteroposterior, 0.5, 0.8, 1.1; mediolateral, 1.1 (for all three injections); and dorsoventral, 2.15, 2.2, 2.25. The micropipette was left in situ for 5 min after injection to allow proper diffusion. Recombinant mouse 3K3A-APC (0.2 mg/kg diluted in saline) or vehicle was administered via tail vein 4 h and 1, 2, 3 and 4 d after stroke (Fig. 1 A).

MRI

MRI was performed using a cryogen-free 7T MRI scanner (MR Solutions) as previously described (Montagne et al., 2018; Nikolakopoulou et al., 2019). All MRI measurements including lesion volume, BBB permeability assessment, and diffusion-weighted imaging (DWI) were performed in vivo. Mice were

anesthetized for the imaging using 2.5% isoflurane/air, and anesthesia was maintained using 1–1.8% isoflurane. Animal temperature (36.5 ± 0.5°C) and breathing rate (80–100 breaths/min) were monitored during anesthesia using a rectal probe and a pressure-sensitive breathing sensor (Small Animal Instruments).

Lesion volumes were measured using a horizontal T2-weighted fast spin-echo sequence (repetition time and time to echo [TR/TE], 4,000/28 ms; 6 averages, field of view [FOV], 14 × 21 × 0.3 mm; and matrix size, 256 × 259). DWI was performed using EPI (TR/TE, 5,000/32 ms; 2 averages; 6 diffusion sampling directions; b-value, 700 s/mm^2; FOV, 25 × 25 × 0.5 mm; and matrix size, 120 × 76). MRI for BBB permeability changes consisted of T1 mapping with variable flip angle method (fast low-angle shot [FLASH]; TR/TE, 31/4 ms; 3 averages; fractional anisotropy [FA], 5–45°; 5 flip angle; FOV, 22 × 22 × 1 mm; and matrix size, 256 × 256) followed by T1-weighted DCE-MRI (FLASH; TR/TE, 31/4 ms; 3 averages; FA, 15°; FOV, 22 × 22 × 1 mm; matrix size, 256 × 256; and number of experiments, 180) with identical geometry, consisting of two horizontal slices to cover infarcted area and one coronal slice for individually selected arterial input function (AIF; Montagne et al., 2018; Nikolakopoulou et al., 2019). Magnevist (gadopentetate dimeglumine contrast agent diluted 1:5 in saline) was injected with a power injector as a bolus of 200 µl in 20 s. Total imaging time was ∼50 min/mouse.

Lesion size

Lesion sizes were measured using ImageJ (National Institutes of Health). The lesion height in coronal direction (equal to slice thickness, 300 µm) was multiplied by the average area measured from two consecutive slices to get lesion volume in cubic millimeters.

BBB permeability assessment

T1 maps and DCE-MRI datasets were processed using our in-house–made Rocketship software running in Matlab environment (Montagne et al., 2018; Nikolakopoulou et al., 2019). T1 relaxation values were measured before gadolinium-diethylenetriamine pentaacetic acid injection with variable flip angle method with constant TR/TE and standard recovery equation. Parametric BBB K_{trans} maps were generated from DCE-MRI scans and measured in a similar way (blood-to-brain transfer constant using linear regression Patlak model, unit × 10^{-3} · min^{-1}) as previously described (Montagne et al., 2018; Nikolakopoulou et al., 2019). We selected arterial input function for each animal from the common carotid artery as in our previous studies (Montagne et al., 2018; Nikolakopoulou et al., 2019).

The total tracer concentration in the tissue, C_{tissue} (t), can be described as a function of the arterial vascular concentration C_{AIF} (t), the intravascular blood volume v_p, and the BBB permeability transfer constant K_{trans} that represents the flow of the tracer from the intravascular to the extravascular space using Eq. 1:

$$C_{tissue}(t) = K_{trans}\int_0^t C_{AIF}(\tau)d\tau + v_p \cdot C_{AIF}(t). \quad (1)$$

BBB permeability values were measured using ImageJ and are reported for the lesion site.

DWI MRI

The reconstruction of EPI-DWI datasets was done using DSI Studio (http://dsi-studio.labsolver.org/) and the DTI reconstruction method with tensor and diffusivity outputs. FA-aided tractography focusing on the fibers in the CC was used. We ran deterministic streamline tractography based on the DTI (1-shell) images, varying the fiber termination parameters. FA was used as a fiber-stopping criterion at threshold 0.2 for the 1-shell images. 6,000 fibers were traced in the selected area of the CC at a maximum fiber turning angle of 60° as previously described (Daianu et al., 2015). For representative EPI-DWI images, restricted diffusion was quantified with a diffusion sampling length ratio of 1.25. A seeding region was placed at the medial CC. The anisotropy threshold was randomly selected. The angular threshold was 30°. The step size was randomly selected as 0.5–1.5 voxels. The fiber trajectories were smoothed by averaging the propagation direction with a percentage of the previous direction. The percentage was randomly selected as 0–95%. Tracks with length <0 or >100 mm were discarded. A total of 5,000 tracts were calculated.

Behavioral tests

In a separate group of mice treated as above with 3K3A-APC or vehicle or sham-operated, we performed behavioral tests. The adhesive removal test was performed to assess sensorimotor deficits as previously described (Wang et al., 2016b). The grid-walking task was performed to test motor control as previously described (Rosenzweig and Carmichael, 2013).

Brain tissue preparation

Mice were anesthetized with 100 mg/kg ketamine and 10 mg/kg xylazine i.p. and transcardially perfused with 30 ml PBS containing 0.005 M EDTA followed by 30 ml of 4% paraformaldehyde (PFA) in PBS. Brains were removed, fixed in 4% PFA, cryoprotected in 30% sucrose in PBS, and sliced into 20-µm-thick coronal sections using a cryostat (CM3050 S; Leica).

Immunohistochemistry

Free-floating brain sections were blocked with 5% normal donkey serum (Vector Laboratories)/0.1%Triton X-100/0.01 M PBS for 1 h and incubated with primary antibodies overnight at 4°C. After incubation with primary antibodies, sections were washed in PBS and incubated with fluorophore-conjugated secondary antibodies in DAPI fluorescence mounting medium (Dako). For a list of primary and secondary antibodies, see Table S1. Sections were imaged with a Zeiss LSM 510 confocal laser-scanning microscope using a series of high-resolution optical sections (1,024 × 1,024-pixel format) that were captured with a 25× water-immersion objective, with 1× zoom at 1-µm-step intervals for Z-stacks. Laser settings for gain, digital offset, and laser intensity were kept standardized between different treatments and experiments. Z-stack projections and pseudo-coloring were performed using Zen software (Carl Zeiss Microimaging). Image postanalysis was performed using ImageJ software. In each animal, five serial 20-µm sections spaced at 200 µm were analyzed across the lesion.

Injury size measurement

Injury size was assessed on coronal sections by Cresyl Violet staining, as previously reported (Wang et al., 2016b). Each section was outlined, and the sum of the areas was integrated to obtain injury volume in cubic millimeters using ImageJ.

Fluorescent intensity analysis of extravascular fibrinogen and IgG deposition

Extravascular fibrinogen and mouse endogenous IgG were detected as previously described (Montagne et al., 2018; Nikolakopoulou et al., 2019). Fibrinogen$^+$ and IgG$^+$ fluorescent signals were determined using ImageJ.

MBP

Quantification of MBP signal was performed as previously described (Montagne et al., 2018). MBP$^+$ signal in the lesion area was subjected to threshold processing and analyzed using ImageJ.

SMI 312

Quantification of SMI 312 signal was performed as previously described (Montagne et al., 2018; Nikolakopoulou et al., 2019). SMI 312$^+$ signal within the lesion area was subjected to threshold processing and analyzed using ImageJ.

Oligodendrocyte counts

10-µm maximum-projection z-stacks were reconstructed. The number of OLs (Olig2$^+$CNPase$^+$) and OPCs (Olig2$^+$PDGFRα$^+$; Baumann and Pham-Dinh, 2001; Montagne et al., 2018) and TUNEL$^+$ OLs and OPCs was determined in the lesion area using the ImageJ cell counter plugin analysis tool (Montagne et al., 2018). Tissue from the same stereotaxic location was used to count OLs and OPCs in sham control animals. Data are normalized as number of cells per square millimeter of the lesion area.

TUNEL

TUNEL$^+$ OLs and OPCs were detected using the in situ death detection kit Fluorescein (Roche Molecular Biochemicals; Montagne et al., 2018). Counting was done as explained in Oligodendrocyte counts.

Microglia and astrocyte counts

10-µm maximum-projection z-stacks were reconstructed. The numbers of Iba1$^+$ microglia and GFAP$^+$ astrocytes were determined using the ImageJ cell counter plugin analysis tool (Nikolakopoulou et al., 2019). Iba1$^+$ microglia were counted within the perilesion area in a 100-µm-wide perimeter around the edge of the infarct (Rosenzweig and Carmichael, 2013). GFAP$^+$ astrocytes were counted throughout the lesion (Sozmen et al., 2019), as reported previously. Data are expressed as number of cells per square millimeter.

Quantitative RT-PCR (RT-qPCR)

Tissue was collected from injury CC site (coordinates range: anteroposterior, 0–1.2 mm; and mediolateral, 0.5–1.5 mm). Relative mRNA abundance of *Tnf-α*, *Il-6*, *Il1-β*, and *Ccl-2* was determined by RT-qPCR. Data were analyzed by normalizing the expression of *Tnf-α*, *Il-6*, *Il1-β*, and *Ccl-2* to *Gapdh* (housekeeping gene). Total RNA was prepared using a RNeasy Plus Universal kit (73404; Qiagen). RT-qPCR amplification was performed using a one-step SYBR green qPCR kit (95087; QuantaBio). Relative abundance was calculated using the $2^{-\Delta Ct}$ method, where Ct (cycle threshold) was defined as the number of cycles required for the fluorescent signal to cross the threshold (i.e., exceed background level), as described previously (Lazic et al., 2019). The following primers were used: for *Tnf-α*: forward, 5′-CTT CTGTCTACTGAACTTCGGG-3′, and reverse, 5′-TGATCTGAG TGTGAGGGTCTG-3′; for *Ccl-2*: forward, 5′-CATCCACGTGTT GGCTCA-3′, and reverse, 5′-GATCATCTTGCTGGTGAATCAGT-3′; and for *Il-6*, *Il1-β*, and *Gapdh*, primers purchased from Bio-Rad (qMmuCID0005613, qMmuCID0005641, and qMmuCED0027 497, respectively).

The expression of PARs was studied in OLs and OPCs, astrocytes, microglia, and neurons. OLs and OPCs were freshly isolated from the WM by FACS as described (Montagne et al., 2018; see FACS below). Primary astrocytes were isolated from postnatal day 1 (P1)–P4 mouse pups and cultured as described (Winkler et al., 2015). Primary neuron cultures were derived from mouse embryos at embryonic day 15.5 and cultured as described (Guo et al., 2004; Guo et al., 2009a; Guo et al., 2009b; Lazic et al., 2019). Primary mouse microglia (M1900-57; ScienCell) were cultured according to the manufacturer's instructions. *F2r*, *F2rl1*, *F2rl2*, and *F2rl3* PrimePCR SYBR Green Assay primers were ordered from Bio-Rad (qMmuCID0006257, qMmuCID0007787, qMmuCID0007819, and qMmuCED0004 073m, respectively). For *Gapdh*, Ct was 16–24; and for *F2r*, *F2rl1*, *F2rl2*, and *F2RL3* genes, Ct was 26–33 for all cell types studied.

Western blotting

Tissues collected from the lesion site and OL, microglia, astrocyte, and neuron cell culture lysates were lysed in radioimmunoprecipitation assay buffer (50 mM Tris, pH 8.0, 150 mM NaCl, 1% NP-40, 0.1% SDS, 0.5% sodium deoxycholate, and Roche protease inhibitor cocktail). The lysates were sonicated and centrifuged at 20,000 *g* for 20 min. The supernatants were used for protein quantification (23228; Thermo Fisher Scientific). Samples were prepared with lithium dodecyl sulfate sample buffer (Invitrogen). Proteins (15 µg) were separated by electrophoresis on NuPAGE Novex Bis-Tris precast 4–12% gradient gels (Thermo Fisher Scientific). After electrophoretic transfer, nitrocellulose membranes (Bio-Rad) were blocked with blocking buffer (37536; Thermo Fisher Scientific) and incubated overnight at 4°C with primary antibodies including mouse anti-human PAR1, cross-reacts with mouse PAR1 (sc-13503; Santa Cruz); rabbit anti-human PAR2, cross-reacts with mouse PAR2 (ab124227; Abcam); rabbit anti-human PAR3, cross-reacts with mouse PAR3 (sc-5598; Santa Cruz); rabbit anti-human PAR4, cross-reacts with mouse PAR4 (PA5-72392; Thermo Fisher Scientific); and rabbit anti-human β-actin, cross-reacts with mouse β-actin (4970S; Cell Signaling). Membranes were then incubated with HRP-conjugated secondary antibodies (HRP-conjugated donkey anti-mouse, 7076S, Cell Signaling, 1:3,000; HRP-conjugated donkey anti-rabbit, A16023, Invitrogen, 1:3,000) for

1 h at room temperature, washed in Tris-buffered saline containing 0.1% Tween 20, and treated for 5 min with Super Signal West Pico chemiluminescent substrate (Thermo Fisher Scientific). Membranes were exposed to CL-XPosure film (Thermo Fisher Scientific) and developed in an X-OMAT 3000 RA film processer (Kodak).

FACS

Animals were transcardially perfused with 0.01 M PBS, and brains were removed. WM tissue (CC, internal capsule, cingulum, and external capsule) was isolated, trypsinized for 30 min with 0.25% trypsin at 37°C, and dissociated using a glass homogenizer, as described (Montagne et al., 2018). Cells were fixed in 4% PFA for 10 min, blocked in 10% NDS/0.1% Triton X-100/1× PBS, and stained for mature OL markers (rabbit proteolipid protein [ab105784; Abcam; 1:2,000] and mouse MBP [SMI-99; BioLegend; 1:500]), OPC marker A2B5 (A8229; Sigma-Aldrich; 1:50), and oligodendrocyte marker Olig2 (AB9610; Millipore; 1:200). This was followed by incubation with secondary antibodies Alexa Fluor 488 (Invitrogen; 1:200) and Alexa Fluor 647 (Invitrogen; 1:200), respectively. Cells were sorted using BD SORP FACSAria I (BD). Gated cells were 95–98% pure.

Silencing of PARs in vitro

Mature OLs were transfected with control or one of the following siRNAs from Dharmacon, *F2r* (E-054176-00-0010), *F2rl1* (E-061445-00-0010), *F2rl2* (E-055946-00-0010), or *F2rl3* (E-062092-00-0010), to knock down PAR1, PAR2, PAR3, and PAR4 expression, respectively, as previously described (Guo et al., 2013). For in vitro studies, 72 h after silencing, OLs were treated with vehicle or 3K3A-APC (5 nM) for 24 h.

Silencing of PARs in vivo

For in vivo PAR1 and PAR3 silencing, we used *F2r*-specific (4457308) and *F2rl2*-specific (4457298) chemically modified 21-mer double-stranded Ambion in vivo siRNA, respectively (Thermo Fisher Scientific). This Ambion technology has established effectiveness and stability, as we reported previously in plasminogen (Montagne et al., 2018) and pleiotrophin (Nikolakopoulou et al., 2019), by showing that ICV delivery of their respective siRNAs effectively suppressed their local gene expression in brain within 24 h of ICV administration, with the effect lasting for >2 wk after a single injection when used with Invivofectamine reagent. Ambion In Vivo siRNA was reconstituted in Invivofectamine 3.0 reagent and diluted in PBS; a final dose of 0.1 nmol in 1 µl was delivered ICV to both lateral ventricles over 5 min using a Hamilton syringe, as previously reported (Montagne et al., 2018; Nikolakopoulou et al., 2019). To confirm the knockdown efficiency, the CC was dissected and prepared for PAR1 and PAR3 immunoblotting 1 wk after ICV siRNA administration. WM stroke was induced 1 wk after PAR1 and PAR3 silencing.

Mouse OL culture

A2B5-positive OPCs were isolated from cortices of C57BL/6J P5 mouse pups by magnetic cell sorting (Miltenyi Biotec), as previously described (Montagne et al., 2018). Brains were removed, minced, and processed using Neural Dissociation Kit (130-092-628; Miltenyi Biotec). After tissue digestion and dissociation, cells were filtered, centrifuged, and resuspended in DMEM (Invitrogen) containing 1% FBS (Hyclone), incubated with blocking reagent and magnetically labeled anti-A2B5 microbeads (130-093-392; Miltenyi Biotec), followed by magnetic sorting using magnetic cell sorting LS columns (130-042-401; Miltenyi Biotec). OPCs were plated at 5 × 10^4 cell density on poly-D-lysine–coated coverslips and allowed to differentiate into mature OLs in medium containing DMEM/Sato supplement–based growth medium, Forskolin, NT3, and T3 (T3 is the active hormone; 3,5,30-tri-iodothyronine; Montagne et al., 2018; Zuchero et al., 2015). Matured OLs were used for OGD and 3K3A-APC experiments.

OGD and 3K3A-APC experiments

OGD was introduced after 7 d in vitro when cultures were ∼90% positive for MBP and negative for O4, a marker for an intermediate transitional cell type (preimmature OLs) between OPCs and mature OLs (Montagne et al., 2018; Zuchero et al., 2015). Cells were cultured in glucose-free DMEM supplemented with 3K3A-APC and transferred in a humidified incubator chamber (Billups-Rothenberg) with 1% O_2 at 37°C for 6 h, as described (Montagne et al., 2018). Cells were then removed from the chamber and processed for immunocytochemistry.

Immunocytochemistry

OLs were detected with an anti-mouse MBP monoclonal antibody (SMI-99; Covance; 1:500) followed by TUNEL and DAPI-Fluoromount-G (SouthernBiotech) staining. Secondary antibody for MBP^+ OLs was donkey anti-mouse Alexa Fluor 568 IgG (Invitrogen; 1:500). OL cell death after OGD was expressed as the percentage of $TUNEL^+MBP^+$ OLs (Montagne et al., 2018).

Statistics

Sample sizes were calculated using NQUERY, assuming a two-sided α-level of 0.05, 80% power, and homogeneous variances for the two samples to be compared with the means and SD from other studies and our previously published studies. Data are presented as mean ± SD. One-way ANOVA followed by Bonferroni's multiple comparison post hoc test was used to determine statistically significant differences. $P < 0.05$ was considered statistically significant.

Online supplemental material

Fig. S1 shows additional representative images 7 d after stroke, supporting Fig. 1. Fig. S2 shows additional representative images 7 d after stroke, supporting Fig. 4. Fig. S3 shows additional representative images 7 d after stroke, supporting Figs. 7 and 8. Table S1 lists primary and secondary antibodies used for immunostaining.

Acknowledgments

This work was supported by National Institutes of Health grants R01NS117827 and R01NS090904 to B.V. Zlokovic and R01HL142975 to J.H. Griffin.

Author contributions: B.V. Zlokovic and J.H. Griffin designed the study. M.T. Huuskonen, Y. Wang, A.M. Nikolakopoulou, A. Montagne, Z. Dai, D. Lazic, and A.P. Sagare conducted experiments and analyzed the data. Z. Zhao analyzed data and help with data presentation. J.A. Fernandez and J.H. Griffin provided reagents. M.T. Huuskonen, Y. Wang, A.M. Nikolakopoulou, A. Montagne, and B.V. Zlokovic prepared the figures. M.T. Huuskonen, Y. Wang, A.M. Nikolakopoulou, and A. Montagne contributed to manuscript writing. B.V. Zlokovic supervised all data analysis and interpretation and wrote the manuscript.

Disclosures: J.H. Griffin reported a patent to US 7,498,305 licensed "ZZ Biotech LLC"; and is a consultant for ZZBiotech LLC. B.V. Zlokovic is a founder of ZZ Biotech LLC, a biotechnology company with a mission to develop APC and its functional mutants for the treatment of stroke and other neurological disorders. No other disclosures were reported.

Submitted: 25 June 2021
Revised: 19 August 2021
Accepted: 29 October 2021

References

Baumann, N., and D. Pham-Dinh. 2001. Biology of oligodendrocyte and myelin in the mammalian central nervous system. *Physiol. Rev.* 81:871–927. https://doi.org/10.1152/physrev.2001.81.2.871

Bos, D., F.J. Wolters, S.K.L. Darweesh, M.W. Vernooij, F. de Wolf, M.A. Ikram, and A. Hofman. 2018. Cerebral small vessel disease and the risk of dementia: A systematic review and meta-analysis of population-based evidence. *Alzheimers Dement.* 14:1482–1492. https://doi.org/10.1016/j.jalz.2018.04.007

Burnier, L., and L.O. Mosnier. 2013. Novel mechanisms for activated protein C cytoprotective activities involving noncanonical activation of protease-activated receptor 3. *Blood.* 122:807–816. https://doi.org/10.1182/blood-2013-03-488957

Cao, C., Y. Gao, Y. Li, T.M. Antalis, F.J. Castellino, and L. Zhang. 2010. The efficacy of activated protein C in murine endotoxemia is dependent on integrin CD11b. *J. Clin. Invest.* 120:1971–1980. https://doi.org/10.1172/JCI40380

Chan, S.J., W. Niu, K. Hayakawa, G. Hamanaka, X. Wang, P.S. Cheah, S. Guo, Z. Yu, K. Arai, M.H. Selim, et al. 2019. Promoting Neuro-Supportive Properties of Astrocytes with Epidermal Growth Factor Hydrogels. *Stem Cells Transl. Med.* 8:1242–1248. https://doi.org/10.1002/sctm.19-0159

Cheng, T., D. Liu, J.H. Griffin, J.A. Fernández, F. Castellino, E.D. Rosen, K. Fukudome, and B.V. Zlokovic. 2003. Activated protein C blocks p53-mediated apoptosis in ischemic human brain endothelium and is neuroprotective. *Nat. Med.* 9:338–342. https://doi.org/10.1038/nm826

Cheng, T., A.L. Petraglia, Z. Li, M. Thiyagarajan, Z. Zhong, Z. Wu, D. Liu, S.B. Maggirwar, R. Deane, J.A. Fernández, et al. 2006. Activated protein C inhibits tissue plasminogen activator-induced brain hemorrhage. *Nat. Med.* 12:1278–1285. https://doi.org/10.1038/nm1498

Daianu, M., R.E. Jacobs, T.M. Weitz, T.C. Town, and P.M. Thompson. 2015. Multi-Shell Hybrid Diffusion Imaging (HYDI) at 7 Tesla in TgF344-AD Transgenic Alzheimer Rats. *PLoS One.* 10:e0145205. https://doi.org/10.1371/journal.pone.0145205

de Leeuw, F.E., J.C. de Groot, E. Achten, M. Oudkerk, L.M. Ramos, R. Heijboer, A. Hofman, J. Jolles, J. van Gijn, and M.M. Breteler. 2001. Prevalence of cerebral white matter lesions in elderly people: a population based magnetic resonance imaging study. The Rotterdam Scan Study. *J. Neurol. Neurosurg. Psychiatry.* 70:9–14. https://doi.org/10.1136/jnnp.70.1.9

Debette, S., and H.S. Markus. 2010. The clinical importance of white matter hyperintensities on brain magnetic resonance imaging: systematic review and meta-analysis. *BMJ.* 341(jul26 1):c3666. https://doi.org/10.1136/bmj.c3666

DeCarli, C., E. Fletcher, V. Ramey, D. Harvey, and W.J. Jagust. 2005. Anatomical mapping of white matter hyperintensities (WMH): exploring the relationships between periventricular WMH, deep WMH, and total WMH burden. *Stroke.* 36:50–55. https://doi.org/10.1161/01.STR.0000150668.58689.f2

GBD 2016 Lifetime Risk of Stroke Collaborators, Feigin, V.L., G. Nguyen, K. Cercy, C.O. Johnson, T. Alam, P.G. Parmar, A.A. Abajobir, K.H. Abate, F. Abd-Allah, et al. 2018. Global, Regional, and Country-Specific Lifetime Risks of Stroke, 1990 and 2016. *N. Engl. J. Med.* 379:2429–2437. https://doi.org/10.1056/NEJMoa1804492

Ghosh, M., M. Balbi, F. Hellal, M. Dichgans, U. Lindauer, and N. Plesnila. 2015. Pericytes are involved in the pathogenesis of cerebral autosomal dominant arteriopathy with subcortical infarcts and leukoencephalopathy. *Ann. Neurol.* 78:887–900. https://doi.org/10.1002/ana.24512

Griffin, J.H., B.V. Zlokovic, and L.O. Mosnier. 2015. Activated protein C: biased for translation. *Blood.* 125:2898–2907. https://doi.org/10.1182/blood-2015-02-355974

Griffin, J.H., L.O. Mosnier, J.A. Fernández, and B.V. Zlokovic. 2016. 2016 Scientific Sessions Sol Sherry Distinguished Lecturer in Thrombosis: Thrombotic Stroke: Neuroprotective Therapy by Recombinant-Activated Protein C. *Arterioscler. Thromb. Vasc. Biol.* 36:2143–2151. https://doi.org/10.1161/ATVBAHA.116.308038

Griffin, J.H., B.V. Zlokovic, and L.O. Mosnier. 2018. Activated protein C, protease activated receptor 1, and neuroprotection. *Blood.* 132:159–169. https://doi.org/10.1182/blood-2018-02-769026

Guo, H., D. Liu, H. Gelbard, T. Cheng, R. Insalaco, J.A. Fernández, J.H. Griffin, and B.V. Zlokovic. 2004. Activated protein C prevents neuronal apoptosis via protease activated receptors 1 and 3. *Neuron.* 41:563–572. https://doi.org/10.1016/S0896-6273(04)00019-4

Guo, H., I. Singh, Y. Wang, R. Deane, T. Barrett, J.A. Fernández, N. Chow, J.H. Griffin, and B.V. Zlokovic. 2009a. Neuroprotective activities of activated protein C mutant with reduced anticoagulant activity. *Eur. J. Neurosci.* 29:1119–1130. https://doi.org/10.1111/j.1460-9568.2009.06664.x

Guo, H., Y. Wang, I. Singh, D. Liu, J.A. Fernández, J.H. Griffin, N. Chow, and B.V. Zlokovic. 2009b. Species-dependent neuroprotection by activated protein C mutants with reduced anticoagulant activity. *J. Neurochem.* 109:116–124. https://doi.org/10.1111/j.1471-4159.2009.05921.x

Guo, H., Z. Zhao, Q. Yang, M. Wang, R.D. Bell, S. Wang, N. Chow, T.P. Davis, J.H. Griffin, S.A. Goldman, and B.V. Zlokovic. 2013. An activated protein C analog stimulates neuronal production by human neural progenitor cells via a PAR1-PAR3-S1PR1-Akt pathway. *J. Neurosci.* 33:6181–6190. https://doi.org/10.1523/JNEUROSCI.4491-12.2013

Han, M.H., S.I. Hwang, D.B. Roy, D.H. Lundgren, J.V. Price, S.S. Ousman, G.H. Fernald, B. Gerlitz, W.H. Robinson, S.E. Baranzini, et al. 2008. Proteomic analysis of active multiple sclerosis lesions reveals therapeutic targets. *Nature.* 451:1076–1081. https://doi.org/10.1038/nature06559

Healy, L.D., J.A. Fernández, L.O. Mosnier, and J.H. Griffin. 2021. Activated protein C and PAR1-derived and PAR3-derived peptides are anti-inflammatory by suppressing macrophage NLRP3 inflammasomes. *J. Thromb. Haemost.* 19:269–280. https://doi.org/10.1111/jth.15133

Henrich-Noack, P., M. Riek-Burchardt, K. Baldauf, G. Reiser, and K.G. Reymann. 2006. Focal ischemia induces expression of protease-activated receptor1 (PAR1) and PAR3 on microglia and enhances PAR4 labeling in the penumbra. *Brain Res.* 1070:232–241. https://doi.org/10.1016/j.brainres.2005.10.100

Hu, X., P. Li, Y. Guo, H. Wang, R.K. Leak, S. Chen, Y. Gao, and J. Chen. 2012. Microglia/macrophage polarization dynamics reveal novel mechanism of injury expansion after focal cerebral ischemia. *Stroke.* 43:3063–3070. https://doi.org/10.1161/STROKEAHA.112.659656

Iadecola, C. 2017. The Neurovascular Unit Coming of Age: A Journey through Neurovascular Coupling in Health and Disease. *Neuron.* 96:17–42. https://doi.org/10.1016/j.neuron.2017.07.030

Iadecola, C., and R.F. Gottesman. 2018. Cerebrovascular Alterations in Alzheimer Disease. *Circ. Res.* 123:406–408. https://doi.org/10.1161/CIRCRESAHA.118.313400

Kapasi, A., C. DeCarli, and J.A. Schneider. 2017. Impact of multiple pathologies on the threshold for clinically overt dementia. *Acta Neuropathol.* 134:171–186. https://doi.org/10.1007/s00401-017-1717-7

Lazic, D., A.P. Sagare, A.M. Nikolakopoulou, J.H. Griffin, R. Vassar, and B.V. Zlokovic. 2019. 3K3A-activated protein C blocks amyloidogenic BACE1 pathway and improves functional outcome in mice. *J. Exp. Med.* 216:279–293. https://doi.org/10.1084/jem.20181035

Liao, F.F., G. Lin, X. Chen, L. Chen, W. Zheng, R. Raghow, F.M. Zhou, A.Y. Shih, and X.L. Tan. 2021. Endothelial Nitric Oxide Synthase-Deficient Mice: A Model of Spontaneous Cerebral Small-Vessel Disease. *Am. J. Pathol.* 191:1932–1945. https://doi.org/10.1016/j.ajpath.2021.02.022

Lin, Y., J.M. Wozniak, N.J. Grimsey, S. Girada, A. Patwardhan, O. Molinar-Inglis, T.H. Smith, J.D. Lapek, D.J. Gonzalez, and J. Trejo. 2020. Phosphoproteomic analysis of protease-activated receptor-1 biased signaling reveals unique modulators of endothelial barrier function. *Proc. Natl. Acad. Sci. USA.* 117:5039–5048. https://doi.org/10.1073/pnas.1917295117

Liu, D., T. Cheng, H. Guo, J.A. Fernández, J.H. Griffin, X. Song, and B.V. Zlokovic. 2004. Tissue plasminogen activator neurovascular toxicity is controlled by activated protein C. *Nat. Med.* 10:1379–1383. https://doi.org/10.1038/nm1122

Liu, Q., R. Radwanski, R. Babadjouni, A. Patel, D.M. Hodis, P. Baumbacher, Z. Zhao, B. Zlokovic, and W.J. Mack. 2019. Experimental chronic cerebral hypoperfusion results in decreased pericyte coverage and increased blood-brain barrier permeability in the corpus callosum. *J. Cereb. Blood Flow Metab.* 39:240–250. https://doi.org/10.1177/0271678X17743670

Lyden, P., H. Levy, S. Weymer, K. Pryor, W. Kramer, J.H. Griffin, T.P. Davis, and B. Zlokovic. 2013. Phase 1 safety, tolerability and pharmacokinetics of 3K3A-APC in healthy adult volunteers. *Curr. Pharm. Des.* 19: 7479–7485. https://doi.org/10.2174/13816128196661312301314 54

Lyden, P., K.E. Pryor, C.S. Coffey, M. Cudkowicz, R. Conwit, A. Jadhav, R.N. Sawyer Jr., J. Claassen, O. Adeoye, S. Song, et al. NeuroNEXT Clinical Trials Network NN104 Investigators. 2019. Final Results of the RHAPSODY Trial: A Multi-Center, Phase 2 Trial Using a Continual Reassessment Method to Determine the Safety and Tolerability of 3K3A-APC, A Recombinant Variant of Human Activated Protein C, in Combination with Tissue Plasminogen Activator, Mechanical Thrombectomy or both in Moderate to Severe Acute Ischemic Stroke. *Ann. Neurol.* 85:125–136. https://doi.org/10.1002/ana.25383

Marin, M.A., and S.T. Carmichael. 2018. Stroke in CNS white matter: Models and mechanisms. *Neurosci. Lett.* 684:193–199. https://doi.org/10.1016/j.neulet.2018.07.039

Marin, M.A., and S.T. Carmichael. 2019. Mechanisms of demyelination and remyelination in the young and aged brain following white matter stroke. *Neurobiol. Dis.* 126:5–12. https://doi.org/10.1016/j.nbd.2018.07.023

Matute, C., M. Domercq, A. Pérez-Samartín, and B.R. Ransom. 2013. Protecting white matter from stroke injury. *Stroke.* 44:1204–1211. https://doi.org/10.1161/STROKEAHA.112.658328

McLaughlin, J.N., M.M. Patterson, and A.B. Malik. 2007. Protease-activated receptor-3 (PAR3) regulates PAR1 signaling by receptor dimerization. *Proc. Natl. Acad. Sci. USA.* 104:5662–5667. https://doi.org/10.1073/pnas.0700763104

Minhas, N., M. Xue, and C.J. Jackson. 2017. Activated protein C binds directly to Tie2: possible beneficial effects on endothelial barrier function. *Cell. Mol. Life Sci.* 74:1895–1906. https://doi.org/10.1007/s00018-016-2440-6

Montagne, A., A.M. Nikolakopoulou, Z. Zhao, A.P. Sagare, G. Si, D. Lazic, S.R. Barnes, M. Daianu, A. Ramanathan, A. Go, et al. 2018. Pericyte degeneration causes white matter dysfunction in the mouse central nervous system. *Nat. Med.* 24:326–337. https://doi.org/10.1038/nm.4482

Mosnier, L.O., A.J. Gale, S. Yegneswaran, and J.H. Griffin. 2004. Activated protein C variants with normal cytoprotective but reduced anticoagulant activity. *Blood.* 104:1740–1744. https://doi.org/10.1182/blood-2004-01-0110

Mosnier, L.O., X.V. Yang, and J.H. Griffin. 2007. Activated protein C mutant with minimal anticoagulant activity, normal cytoprotective activity, and preservation of thrombin activable fibrinolysis inhibitor-dependent cytoprotective functions. *J. Biol. Chem.* 282:33022–33033. https://doi.org/10.1074/jbc.M705824200

Mosnier, L.O., R.K. Sinha, L. Burnier, E.A. Bouwens, and J.H. Griffin. 2012. Biased agonism of protease-activated receptor 1 by activated protein C caused by noncanonical cleavage at Arg46. *Blood.* 120:5237–5246. https://doi.org/10.1182/blood-2012-08-452169

Nikolakopoulou, A.M., A. Montagne, K. Kisler, Z. Dai, Y. Wang, M.T. Huuskonen, A.P. Sagare, D. Lazic, M.D. Sweeney, P. Kong, et al. 2019. Pericyte loss leads to circulatory failure and pleiotrophin depletion causing neuron loss. *Nat. Neurosci.* 22:1089–1098. https://doi.org/10.1038/s41593-019-0434-z

Rosenzweig, S., and S.T. Carmichael. 2013. Age-dependent exacerbation of white matter stroke outcomes: a role for oxidative damage and inflammatory mediators. *Stroke.* 44:2579–2586. https://doi.org/10.1161/STROKEAHA.113.001796

Russo, A., U.J. Soh, M.M. Paing, P. Arora, and J. Trejo. 2009. Caveolae are required for protease-selective signaling by protease-activated receptor-1. *Proc. Natl. Acad. Sci. USA.* 106:6393–6397. https://doi.org/10.1073/pnas.0810687106

Schuepbach, R.A., J. Madon, M. Ender, P. Galli, and M. Riewald. 2012. Protease-activated receptor-1 cleaved at R46 mediates cytoprotective effects. *J. Thromb. Haemost.* 10:1675–1684. https://doi.org/10.1111/j.1538-7836.2012.04825.x

Shi, Y., S.T. Hung, G. Rocha, S. Lin, G.R. Linares, K.A. Staats, C. Seah, Y. Wang, M. Chickering, J. Lai, et al. 2019. Identification and therapeutic rescue of autophagosome and glutamate receptor defects in C9ORF72 and sporadic ALS neurons. *JCI Insight.* 5:e127736. https://doi.org/10.1172/jci.insight.127736

Siegel, J.S., L.E. Ramsey, A.Z. Snyder, N.V. Metcalf, R.V. Chacko, K. Weinberger, A. Baldassarre, C.D. Hacker, G.L. Shulman, and M. Corbetta. 2016. Disruptions of network connectivity predict impairment in multiple behavioral domains after stroke. *Proc. Natl. Acad. Sci. USA.* 113: E4367–E4376. https://doi.org/10.1073/pnas.1521083113

Sinha, R.K., X.V. Yang, J.A. Fernández, X. Xu, L.O. Mosnier, and J.H. Griffin. 2016. Apolipoprotein E Receptor 2 Mediates Activated Protein C-Induced Endothelial Akt Activation and Endothelial Barrier Stabilization. *Arterioscler. Thromb. Vasc. Biol.* 36:518–524. https://doi.org/10.1161/ATVBAHA.115.306795

Sinha, R.K., Y. Wang, Z. Zhao, X. Xu, L. Burnier, N. Gupta, J.A. Fernández, G. Martin, S. Kupriyanov, L.O. Mosnier, et al. 2018. PAR1 biased signaling is required for activated protein C in vivo benefits in sepsis and stroke. *Blood.* 131:1163–1171. https://doi.org/10.1182/blood-2017-10-810895

Soh, U.J., and J. Trejo. 2011. Activated protein C promotes protease-activated receptor-1 cytoprotective signaling through β-arrestin and dishevelled-2 scaffolds. *Proc. Natl. Acad. Sci. USA.* 108:E1372–E1380. https://doi.org/10.1073/pnas.1112482108

Sozmen, E.G., A. Kolekar, L.A. Havton, and S.T. Carmichael. 2009. A white matter stroke model in the mouse: axonal damage, progenitor responses and MRI correlates. *J. Neurosci. Methods.* 180:261–272. https://doi.org/10.1016/j.jneumeth.2009.03.017

Sozmen, E.G., S. Rosenzweig, I.L. Llorente, D.J. DiTullio, M. Machnicki, H.V. Vinters, L.A. Havton, R.J. Giger, J.D. Hinman, and S.T. Carmichael. 2016. Nogo receptor blockade overcomes remyelination failure after white matter stroke and stimulates functional recovery in aged mice. *Proc. Natl. Acad. Sci. USA.* 113:E8453–E8462. https://doi.org/10.1073/pnas.1615322113

Sozmen, E.G., D.J. DiTullio, S. Rosenzweig, J.D. Hinman, S.P. Bridges, M.A. Marin, R. Kawaguchi, G. Coppola, and S.T. Carmichael. 2019. White Matter Stroke Induces a Unique Oligo-Astrocyte Niche That Inhibits Recovery. *J. Neurosci.* 39:9343–9359. https://doi.org/10.1523/JNEUROSCI.0103-19.2019

Stavenuiter, F., and L.O. Mosnier. 2014. Noncanonical PAR3 activation by factor Xa identifies a novel pathway for Tie2 activation and stabilization of vascular integrity. *Blood.* 124:3480–3489. https://doi.org/10.1182/blood-2014-06-582775

Uchida, H., H. Sakata, M. Fujimura, K. Niizuma, Y. Kushida, M. Dezawa, and T. Tominaga. 2015. Experimental model of small subcortical infarcts in mice with long-lasting functional disabilities. *Brain Res.* 1629:318–328. https://doi.org/10.1016/j.brainres.2015.10.039

Vanlandewijck, M., L. He, M.A. Mäe, J. Andrae, K. Ando, F. Del Gaudio, K. Nahar, T. Lebouvier, B. Laviña, L. Gouveia, et al. 2018. A molecular atlas of cell types and zonation in the brain vasculature. *Nature.* 554:475–480. https://doi.org/10.1038/nature25739

Walker, C.T., A.H. Marky, A.L. Petraglia, T. Ali, N. Chow, and B.V. Zlokovic. 2010. Activated protein C analog with reduced anticoagulant activity improves functional recovery and reduces bleeding risk following controlled cortical impact. *Brain Res.* 1347:125–131. https://doi.org/10.1016/j.brainres.2010.05.075

Wang, Y., C. Richter-Landsberg, and G. Reiser. 2004. Expression of protease-activated receptors (PARs) in OLN-93 oligodendroglial cells and mechanism of PAR-1-induced calcium signaling. *Neuroscience.* 126: 69–82. https://doi.org/10.1016/j.neuroscience.2004.03.024

Wang, Y., Z. Zhang, N. Chow, T.P. Davis, J.H. Griffin, M. Chopp, and B.V. Zlokovic. 2012. An activated protein C analog with reduced anticoagulant activity extends the therapeutic window of tissue plasminogen activator for ischemic stroke in rodents. *Stroke.* 43:2444–2449. https://doi.org/10.1161/STROKEAHA.112.658997

Wang, Y., Z. Zhao, N. Chow, P.S. Rajput, J.H. Griffin, P.D. Lyden, and B.V. Zlokovic. 2013. Activated protein C analog protects from ischemic stroke and extends the therapeutic window of tissue-type plasminogen activator in aged female mice and hypertensive rats. *Stroke.* 44: 3529–3536. https://doi.org/10.1161/STROKEAHA.113.003350

Wang, Y., G. Liu, D. Hong, F. Chen, X. Ji, and G. Cao. 2016a. White matter injury in ischemic stroke. *Prog. Neurobiol.* 141:45–60. https://doi.org/10.1016/j.pneurobio.2016.04.005

Wang, Y., Z. Zhao, S.V. Rege, M. Wang, G. Si, Y. Zhou, S. Wang, J.H. Griffin, S.A. Goldman, and B.V. Zlokovic. 2016b. 3K3A-activated protein C stimulates postischemic neuronal repair by human neural stem cells in mice. *Nat. Med.* 22:1050–1055. https://doi.org/10.1038/nm.4154

Wardlaw, J.M., M.C. Valdés Hernández, and S. Muñoz-Maniega. 2015. What are white matter hyperintensities made of? Relevance to vascular cognitive impairment. *J. Am. Heart Assoc.* 4:001140. https://doi.org/10.1161/JAHA.114.001140

Wardlaw, J.M., C. Smith, and M. Dichgans. 2019. Small vessel disease: mechanisms and clinical implications. *Lancet Neurol.* 18:684–696. https://doi.org/10.1016/S1474-4422(19)30079-1

Williams, P.D., B.V. Zlokovic, J.H. Griffin, K.E. Pryor, and T.P. Davis. 2012. Preclinical safety and pharmacokinetic profile of 3K3A-APC, a novel, modified activated protein C for ischemic stroke. *Curr. Pharm. Des.* 18:4215–4222. https://doi.org/10.2174/138161212802430413

Winkler, E.A., J.D. Sengillo, A.P. Sagare, Z. Zhao, Q. Ma, E. Zuniga, Y. Wang, Z. Zhong, J.S. Sullivan, J.H. Griffin, et al. 2014. Blood-spinal cord barrier disruption contributes to early motor-neuron degeneration in ALS-model mice. *Proc. Natl. Acad. Sci. USA.* 111:E1035–E1042. https://doi.org/10.1073/pnas.1401595111

Winkler, E.A., Y. Nishida, A.P. Sagare, S.V. Rege, R.D. Bell, D. Perlmutter, J.D. Sengillo, S. Hillman, P. Kong, A.R. Nelson, et al. 2015. GLUT1 reductions exacerbate Alzheimer's disease vasculo-neuronal dysfunction and degeneration. *Nat. Neurosci.* 18:521–530. https://doi.org/10.1038/nn.3966

Yoon, H., M. Radulovic, K.L. Drucker, J. Wu, and I.A. Scarisbrick. 2015. The thrombin receptor is a critical extracellular switch controlling myelination. *Glia.* 63:846–859. https://doi.org/10.1002/glia.22788

Zeisel, A., A.B. Muñoz-Manchado, S. Codeluppi, P. Lönnerberg, G. La Manno, A. Juréus, S. Marques, H. Munguba, L. He, C. Betsholtz, et al. 2015. Brain structure. Cell types in the mouse cortex and hippocampus revealed by single-cell RNA-seq. *Science.* 347:1138–1142. https://doi.org/10.1126/science.aaa1934

Zeisel, A., H. Hochgerner, P. Lönnerberg, A. Johnsson, F. Memic, J. van der Zwan, M. Häring, E. Braun, L.E. Borm, G. La Manno, et al. 2018. Molecular Architecture of the Mouse Nervous System. *Cell.* 174:999–1014.e22. https://doi.org/10.1016/j.cell.2018.06.021

Zhang, Y., K. Chen, S.A. Sloan, M.L. Bennett, A.R. Scholze, S. O'Keeffe, H.P. Phatnani, P. Guarnieri, C. Caneda, N. Ruderisch, et al. 2014. An RNA-sequencing transcriptome and splicing database of glia, neurons, and vascular cells of the cerebral cortex. *J. Neurosci.* 34:11929–11947. https://doi.org/10.1523/JNEUROSCI.1860-14.2014

Zheng, J.J., K. Delbaere, J.C. Close, P.S. Sachdev, and S.R. Lord. 2011. Impact of white matter lesions on physical functioning and fall risk in older people: a systematic review. *Stroke.* 42:2086–2090. https://doi.org/10.1161/STROKEAHA.110.610360

Zhong, Z., H. Ilieva, L. Hallagan, R. Bell, I. Singh, N. Paquette, M. Thiyagarajan, R. Deane, J.A. Fernandez, S. Lane, et al. 2009. Activated protein C therapy slows ALS-like disease in mice by transcriptionally inhibiting SOD1 in motor neurons and microglia cells. *J. Clin. Invest.* 119:3437–3449. https://doi.org/10.1172/JCI38476

Zlokovic, B.V., C. Zhang, D. Liu, J. Fernandez, J.H. Griffin, and M. Chopp. 2005. Functional recovery after embolic stroke in rodents by activated protein C. *Ann. Neurol.* 58:474–477. https://doi.org/10.1002/ana.20602

Zuchero, J.B., M.M. Fu, S.A. Sloan, A. Ibrahim, A. Olson, A. Zaremba, J.C. Dugas, S. Wienbar, A.V. Caprariello, C. Kantor, et al. 2015. CNS myelin wrapping is driven by actin disassembly. *Dev. Cell.* 34:152–167. https://doi.org/10.1016/j.devcel.2015.06.011

Supplemental material

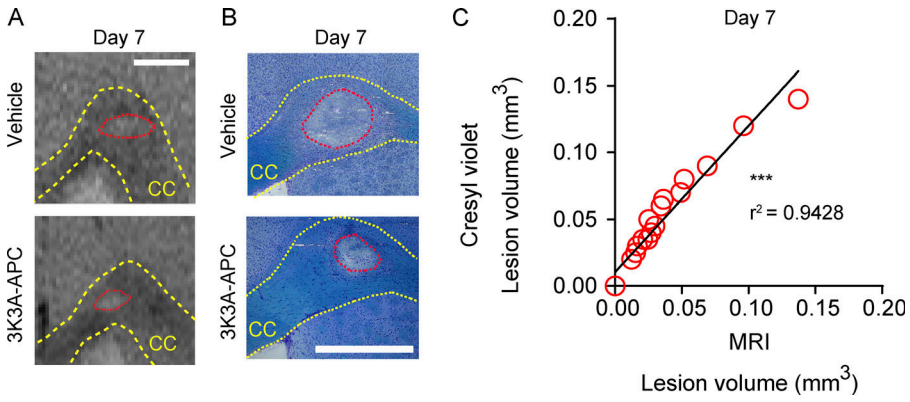

Figure S1. **3K3A-APC reduces lesion volume 7 d after WM stroke. (A)** Representative T2-weighted MRI images of lesion CC site 7 d after stroke. **(B)** Representative images of Cresyl Violet stain on brain coronal sections 7 d after stroke. **(C)** Correlation between lesion volume determined by MRI and Cresyl Violet stain 7 d after stroke. Pearson's correlation was used for statistical testing. In A and B, scale bar = 500 µm. ***, P < 0.001. Supports Fig. 1.

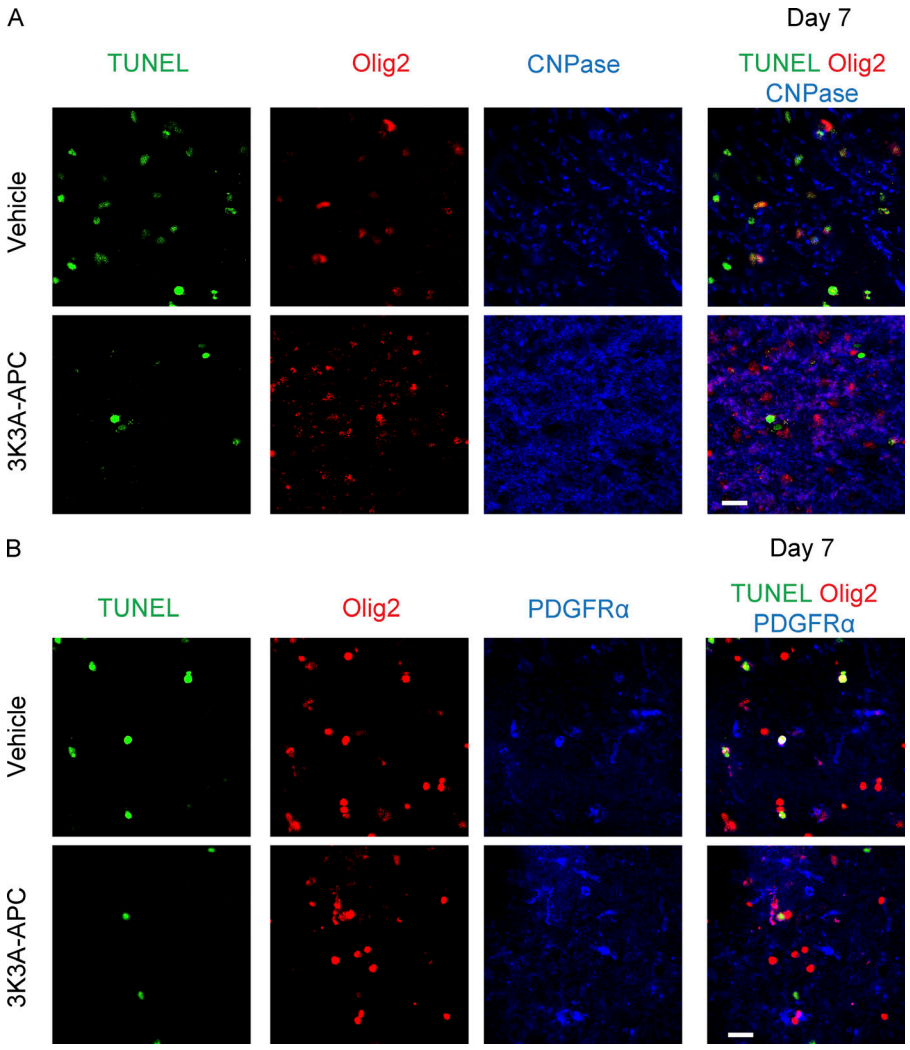

Figure S2. **3K3A-APC protects oligodendrocytes from ischemic injury 7 d after stroke. (A)** Representative images of Olig2 and CNPase immunostaining and TUNEL staining at the lesion site 7 d after WM stroke. **(B)** Representative images of Olig2 and PDGFRα immunostaining and TUNEL staining at the lesion site 7 d after WM stroke. Scale bar, 20 µm. Supports Fig. 4.

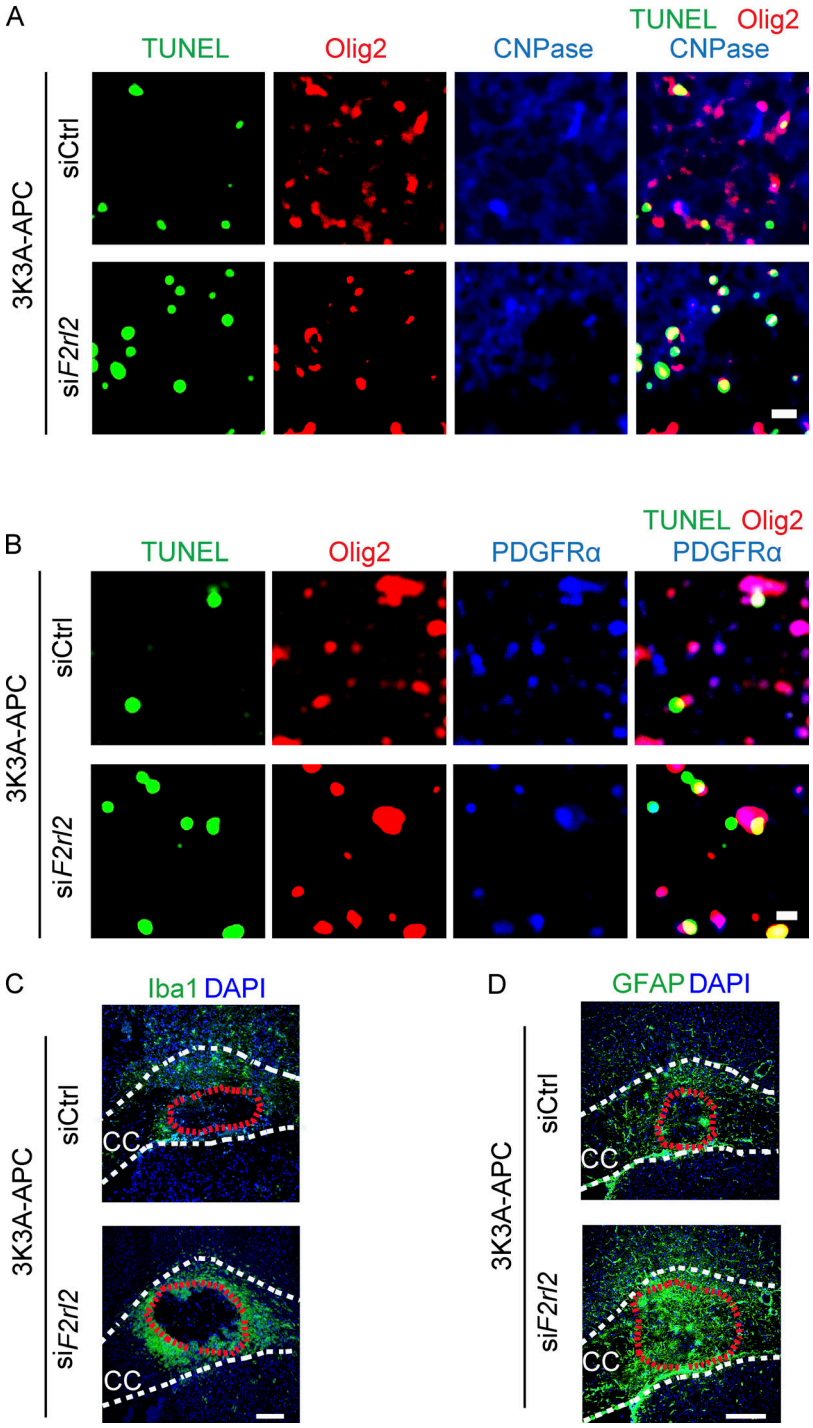

Figure S3. **PAR3 silencing inhibits 3K3A-APC's protection of oligodendrocytes and abolishes 3K3A-APC's suppression of microglia and astrocyte response after WM stroke. (A)** Representative images of Olig2, CNPase, and TUNEL staining at the lesion site in the CC in 3K3A-APC–treated mice after PAR3 silencing or si*Ctrl* on day 1 after stroke. **(B)** Representative images of Olig2, PDGFRα, and TUNEL staining at the CC lesion site in 3K3A-APC–treated after PAR3 silencing or si*Ctrl* on day 1 after stroke. In A and B, scale bar = 20 µm. **(C)** Representative images of Iba1$^+$ microglia in the perilesion area in the CC in 3K3A-APC–treated mice after PAR3 silencing or si*Ctrl* on day 1 after stroke. **(D)** Representative images of GFAP$^+$ astrocytes at the CC lesion site in 3K3A-APC–treated mice after PAR3 silencing or si*Ctrl* on day 1 after stroke. In C and D, scale bar = 100 µm. PAR1 and PAR3 silencing was by ICV delivery of si*F2r* and si*F2rl2*, respectively, or si*Ctrl*, as in Fig. 7. Supports Figs. 7 and 8.

Provided online is one table. Table S1 lists antibodies used for immunohistochemical analyses.